A proposal of building new muon small wheels : the NSW project

Draft XYZ.00   20.01.2012 — TGC + MDT

Abstract

abstract

1 Introduction [TK]

We propose to build a pair of new small wheel detector (NSW) to replace the existing ones during the second long shutdown[1] of the LHC during which the LHC will be upgraded to achieve its luminosity beyond the nominal design value and up to 2-3×10^{34} cm^{-2}s^{-1} in the following running period. The goal of NSW is to bring a significant enhancement of the muon performance in the endcap region, in particular of the level-1 muon trigger as well as the precision muon tracking, that would not be achieved by simple and thus lower cost modifications alone such as improvement of radiation shielding, addition of new detector layers or upgrade of electronics.

The muon small wheel is a part of the ATLAS muon spectrometer located in the endcap region in front of the endcap toroidal magnet. This is the innermost station of the three muon stations of the endcap. There are two identical sets of detectors in both sides of ATLAS. The small wheel consists of 4+4 layers of monitored drift tubes (MDT) for precision tracking in the bending direction (R direction) and two layers of thin gap chambers (TGC) for azimuthal coordinates. These detectors cover the η range of $1.3 < |\eta| < 2.0$. The inner part of the small wheel is covered by four layers of cathode readout chambers (CSC) because of its high rate capability. Each CSC layers determines both bending and azimuthal coordinates. The coverage of the CSC chambers is $2.0 < |\eta| < 2.7$.

Just to check if reference works [1]. Once more to see the order is OK [2].

2 Upgrade motivations [TK]

Discussion of muon spectrometer performance at high luminosity - precision tracking and L1 trigger, and conclude that new detector and electronics are needed.

Point out serious (?) performance degradation in the small wheel region in both MDT and CSC, referring to the radiation background discussoin in Appendix. Performance of the present

---

[1] Currently it is foreseen in 2018.

detector should be evaluated for high lumi conditin, either using high lumi Monte Carlo or overlay of real events. CSC is 4 layers.

In the L1 discussion, emphasise the importance of maintaining low p_T threshold. There are two issues. the high rate of fake triggers in the endcap region based mainly on the study using data. Then introduce basic idea of how this can be mitigated by integrating the small wheel in the L1 trigger. As the second point of trigger, discuss the pT resolution and possible improvement using the new small wheel. Physics requirement asks low pT threshold (20-40 GeV), L1 rate should be maintained at 100 kHz. Need sharpening pT threshold. Here introduce 1 mrad requirement.

Finally conclude that NSW should be built and replace the present ones as a phase-1 upgrade item in preparation to running with luminosity beyond the nominal luminosity.

3 Requirements for the new small wheel [LP]

A short section with short subsections, summarising lists of requirements in numbers.

3.1 Tracking

Segment reconstruction with required performance. Resolution, efficiency, fake, ...

3.2 L1 trigger

Real-time segment reconstruction with required performance. Resolution, efficiency, fakes, ... Delay of signal availability.

3.3 Detector ageing

Integrated dose, Detector (and electronics) has to survive, or foresee replacement.

4 General Detector ..... [JD]

There are n proposed detector concepts which are discussed in next sections. Here, the following 3 points can be discussed commonly.

4.1 Mechanical structure

8+8 large-small layout, total space in z and R. Support structure, accessibility, ..

4.2 Radiation shielding

The same as now, or possible improvement of radiation shielding, ..

4.3 Alignment

Requirements, target figures, important comments which can be made independent of the detail of detector layout.

4.4 Readout electronics

Issues common to all concept. Around ROD.

4.5 DCS, services,

5 Detector concept 1 : Integrated MDT-TGC System

5.1 Introduction

The dominant motivation behind the present proposal is to considerably increase the performance and rate capability of the triggering and precision tracking system in the Small Wheel in order to match the higher background levels in the Phase II upgrade scenario of the LHC.

For this purpose, we propose the following layout for the upgrade of the Small Wheel.

(a) a new type of TGC trigger chamber, providing considerably improved spatial resolution in the bending plane but preserving the basic rugged structure together with the operating parameters of the proven TGC system, as presently installed in the muon end-cap.

(b) a new type of MDT chamber, made from tubes of half the diameter of the presently used tubes, otherwise operating under the same conditions with respect to gas gain, gas composition and pressure. The reduction of the tube diameter from 30 to 15 mm leads to an increase of the rate capability of the tubes by a factor of seven, sufficient to cope with the level of background hits expected at the SLHC.
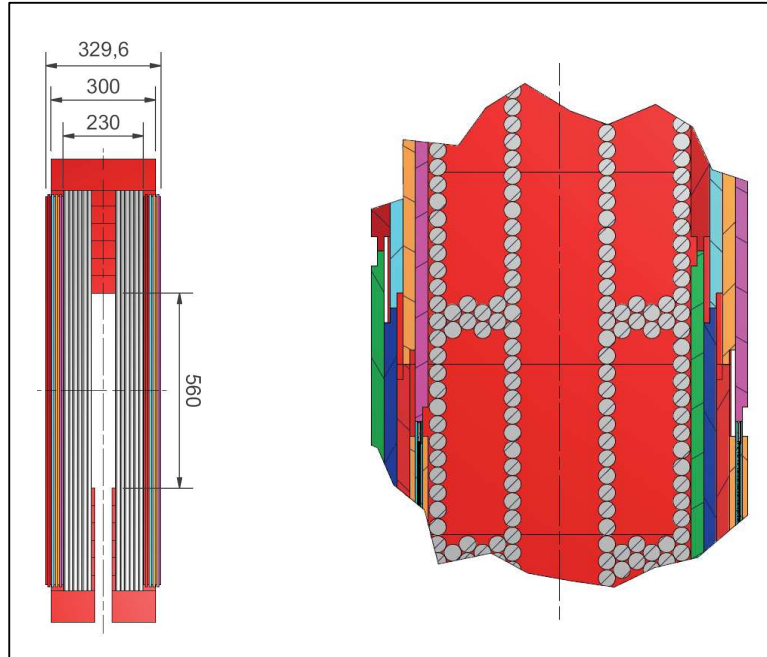

Figure 1: Cross section through the proposed arrangement of trigger TGCs and precision MDTs. The MDT, made out of two multilayers (with 4 or 6 tube layers) is sandwiched between two packages of 4-layer TGCs. The distance of 300 mm between the TGC packages is instrumental for the angular resolution of the triggering muon track.

With this upgrade of the existing chamber technology towards higher performance the uniformity of the present muon spectrometer (MDT as tracking detectors, RPC as trigger

detectors in the barrel and TGCs in the end-cap) is preserved while taking advantage of the existing technical infrastructure and the experience in constructing such an assembly at the relevant institutions.

For the trigger chambers we propose to maintain the basic operating concept of TGC chambers, complementing them with a new, high-performance trigger system. The pulseheight distribution of signals induced into the strips of the TGC cathodes (measuring η) are processed to give the precision coordinate with an accuracy of $< 100 \, \mu m$. To distinguish the new TGCs, proposed for the New Small Wheel (NSW) from the existing ones in the Big Wheel, we will refer to them as to "sTGCs" throughout this article.

In the proposed detector layout, one package of four sTGC chambers is placed in front and one behind the MDT chambers (Fig. 1). A sTGC package will contain four wire layers (wires running radially, perpendicular to the strips), four cathode layers for centroid finding and another four cathode layers, segmented into pads, for fast selection of a trigger tower of interest. Centroids are found for those strips in the trigger tower. Also, in the offline analysis the pads will be an important tool for resolving ambiguities in the x-y pairing of coordinates, when more than one track is present in a chamber.

One important limitation of the present L1-trigger in the end-cap is due to the fact that a majority of tracks, crossing the Small Wheel, do not originate from the primary vertex and should therefore not be considered candidates for a high-p_T muon by the triggering system. The present trigger, however, can not determine the slope of the candidate track in the r-z plane and for this reason is unable to discard tracks not coming from the primary vertex. With a distance of about 300 mm between the sTGC packages in front and behind the MDT, an angular resolution of $\sim 0.4 \, \mathrm{mrad}$ (including multiple scattering) can be achieved, which allows to discard tracks not pointing to the primary vertex from the L1 trigger decision. In addition to the precise measurement of the slope in the η-direction, the slope of in the ϕ direction will also be determined, though with less accuracy, to further reduce the number of false triggers. A detailed presentation of the method is given in section 5.2.1.

The limitations of the MDT precision chambers at high luminosity are mainly caused by isolated hits in the tubes ("fake hits"), coming from neutron and gamma conversions in nearby support structures, tube walls, chamber gas and tungsten wires. The presently used 30 mm diameter tubes ("Large tubes") start to lose efficiency if hit rates go beyond about 300 kHz per tube and, therefore, a new MDT chamber type with half the tube diameter is proposed, leading to seven times higher rate capability.

Both new chamber systems, the sTGCs and the MDTs, can be operated with the same chamber gas as in the present system. Power requirements for the electronics of both systems will be higher due to higher channel count. Whether this requires active cooling, as is the case for the electronics of the CSC chambers in the region $\eta > 2$ is under study. Aim is to have services arranged in such a way as to be able to use the existing service infrastructure like e.g. the flexible chains ("cable Schlepps").

In the present architecture of the Muon spectrometer the precise tracking coordinates of the MDT are not used for the Level-1 trigger, precision and trigger chambers being read out separately and in an asynchronous way. The MDT information is only used at Level-2, where it is instrumental in discarding the majority of Level-1 muon triggers, which may either be

caused by muons with too low p_T or by tracks not pointing to the vertex. To capitalize on the Level-2 selection method already at Level-1, it has been proposed to implement a fast readout path into the MDT readout architecture, making the accurate MDT coordinates available to the trigger logic, early enough for use in the L1 trigger decision. A more detailed discussion of the proposed concepts for L1 trigger sharpening with MDTs is given in section 5.1.3 and in appendix F.

5.1.1   Upgrade of the TGC System

The basis of the proposed concept is to have as many as possible accurate measurements in the trigger layers, to allow discarding a high percentage of measurements where δ-rays, additional γ's or neutrons are present and still obtain a position measurement from each of the two packages with a precision of $100\,\mu m$. To obtain such a precision using the 3.5 mm pitch strips present in each gas-gap, while keeping simple electronics, a method using Time-Over-Threshold as an estimate of charge has been developed. The achieved performance using this method for large size sTGCs is discussed in detail in section 5.2.

Achieving this high accuracy for the bending coordinate in each gas gap provides a valuable complement to the MDT position measurements, similar in precision, reducing the required number of tube layers in the MDT necessary for an unambiguous track identification at high background rates. In particular, in the high background rate region of the Small Wheel, having a total of 20 potential measurement points, of which up to 30% may have to be discarded, ensures that an accurate particle vector will be provided in front of the End-Cap Toroidal field, even if some of the layers become non-operational during the exploitation of ATLAS at SLHC. The overall signal processing to produce the trigger is schematically shown in figure 42 of appendix (C.1). A demonstrator to study the signal path, logics and latency in detail has recently been completed.

By making a coincidence among the pads in a tower of successive layers (within a 1 degree aperture), one is able to substantially reduce the number of channels that have to be read out for a fast trigger decision. Furthermore, the pad-coincidence provides a unique 3-D address, where a corresponding angle and displacement comparison can be made with the trigger input from the existing muon end-cap trigger, originating from the ATLAS Big Wheels. To simplify the logic of what channels to read for trigger purposes, one might loose some of the potential muon candidates.

The MDTs provide, furthermore, an accurate alignment that can be used for precisely aligning the TGC positions by means of tracks.

5.1.2 Upgrade of the MDT System

The large majority of hits in the Monitored Drift Tube (MDT) chambers are caused by Compton scattering of γ's which, in turn, come from neutron capture in the material of the chambers and adjacent support material. The resulting hit densities strongly increase towards the inner radius of the Small Wheels, while, on the other hand, the length of the tubes in the trapezoidal geometry of the SW decreases proportional to the distance from the beam line (r). Hit densities, however, are increasing considerably faster than with 1/r, and therefore the highest tube hit rates are at the innermost radii of the chambers.
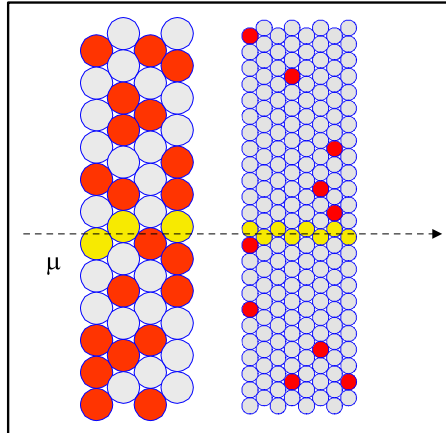

Figure 2: The tracking performance of 15 mm with respect to 30 mm diameter drift tube chambers at high n/γ background rates. An occupancy of 50% in 30 mm diameter tubes (left) due to background hits (red dots) corresponds to only 6% occupancy in the 15 mm diameter tubes (right) due to the 3.9 times shorter drift time and the 2 times smaller cross section.

Reduction of the drift-tube diameter from 30 mm to 15 mm, while keeping the other parameters unchanged (gas composition and gain, sense wire diameter and tube wall thickness) leads to a vast improvement of the rate capability of the drift-tube chambers, exceeding the requirements for operation in the NSW up to the highest conceivable background rates (see illustration in Fig. 2).

Chamb. type	Tube layers	Location in r	Tube length	Expected hit rate	Count rate per tube	Occup-ancy	Tube effi-ciency	Segment efficiency
		cm	cm	Hz/cm^2	kHz	%	%	%
EIL0	2×6	93	56	14000	1176	23,5	79,0	99.9
EIL1	2×4	208	125	5150	965	19,3	82,4	99.9
EIL2	2×4	318	179	1978	530	10,6	90,0	99.9

Table 1: Expected hit rates and efficiencies for 15 mm tubes in a large sector of the NSW. In col. 3 the radial location of the innermost tube of each chamber and in cols. 4 to 8 the tube lengths, the expected hit rates, the counting rates per tube, the occupancies and the 3σ single-tube and the track segment reconstruction efficiencies of a chamber are given for the tubes with highest counting rate at a luminosity of 5 × nominal (times a factor of 1.4, see text).

Table 1 presents tube hit rates, occupancies and efficiencies for the innermost tubes of the three chambers in a Large Sector of the NSW. Chamber EIL0 covers the area now taken by the

7

CSC chambers. The numbers in col. 4 are based on hit rate measurements at a luminosity of $9 \cdot 10^{32}$ cm^{-2}s^{-1}, scaled up linearly to $5 \cdot 10^{34}$ cm^{-2}s^{-1}. Rates in the CSC region (1 m$<$r$<$2 m) are extrapolated from larger radii, using an exponential law [23]. In addition, these rates have been multiplied by a factor of 1.4 in order to increase rates to the 14 kHz/cm^2 specification of this Technical Proposal. This factor of 1.4 could also be considered an additional safety factor in case the real rates will increase faster than predicted by the extrapolation. The efficiencies are calculated from exp(-τ·f) $\approx$ 1-τ·f, where τ is the dead time after a hit (we use as the minimal adjustable value the maximum drift time of 200 ns) and f the hit rate per tube.

Being able to use the drift tubes as tracking devices at very high background rates allows to preserve the main advantages of MDT concept:

(a) High pattern recognition and tracking efficiency up to high backround rates.

(b) High position and angular resolution, independent of the angle of incidence onto the chamber plane. This property of drift tube chambers with their *circular* drift geometry is a decisive advantage over drift chambers with *rectangular* drift geometry.

(c) Operational independence of the drift tubes, where a malfunction of any individual tube can only generate a negligible inefficiency.

(d) Modularity and mechanical robustness of chamber construction.

(e) Direct connection of the high intrinsic mechanical precision of the chambers to the global optical alignment system.

(f) Extensive experience in the construction, quality assurance and operation of the MDT chambers in ATLAS; easy integration into the DAQ, trigger and muon reconstruction chains.

For the standard MDT gas mixture of Ar:CO$_2$ (93:7) at 3 bar absolute pressure, the gas gain of $2 \cdot 10^4$ is achieved at an operating voltage of 2730 V for 15 mm diameter drift tubes (Table 9). Under these operating conditions, the maximum drift time is reduced by a factor of 3.8 from about 700 ns to 185 ns [15]. In addition, the background flux, hitting a tube of given length is reduced by a factor of two. Altogether, the drift-tube occupancy is thus reduced by a factor of 7.6. At the benchmark background rate of 14 kHz/cm^2 at the inner bore of the NSW, corresponding to a counting rate of 1176 kHz in 0.55 m long tubes, the maximum drift tube occupancy is 23% (cf. Table 1).

The proposed layout with 2×6 drift-tube layers at radii $R < 220$ cm in the NSW and with 2×4 layers at larger radii provides very robust tracking with track segment reconstruction efficiencies above 99% [18] and a sMDT chamber spatial resolution of better than 45 μm for $R > 160$ cm and of better than 60 μm at smaller radii at the highest background rates corresponding to 14 kHz/cm^2 at the inner bore of the NSW (see Fig. 28). As also shown in Fig. 28, the combined sTGC-sMDT system provides a spatial resolution of better than 40 μm for the whole NSW.

The mechanical structure and the alignment system will be similar to the present Small Wheel architecture. The sTGC and sMDT chambers will be mechanically aligned in the integrated chamber modules with an accuracy of better than 20 mum. Like in the case of the trigger chambers, new readout electronics with higher rate capability has to be installed (see section 5.5).

5.1.3   Combination of MDT and TGC information to sharpen the trigger

In the present architecture of the Muon spectrometer, trigger and precision chambers operate independently. The information of both chamber systems is read out separately, and the precise tracking coordinates of the MDT are only used at Level-2, where the majority of candidate triggers is discarded, being either caused by tracks with p_T below threshold or by non-projective tracks (not pointing to the vertex). To capitalize on this trigger sharpening already at Level-1, it has been proposed to implement a second, fast readout path, parallel to the existing one, into the MDT readout architecture. This "fast lane" should supply MDT tracking information in a synchroneous way with BX, making the accurate MDT coordinates available to the trigger logic at a very early stage.
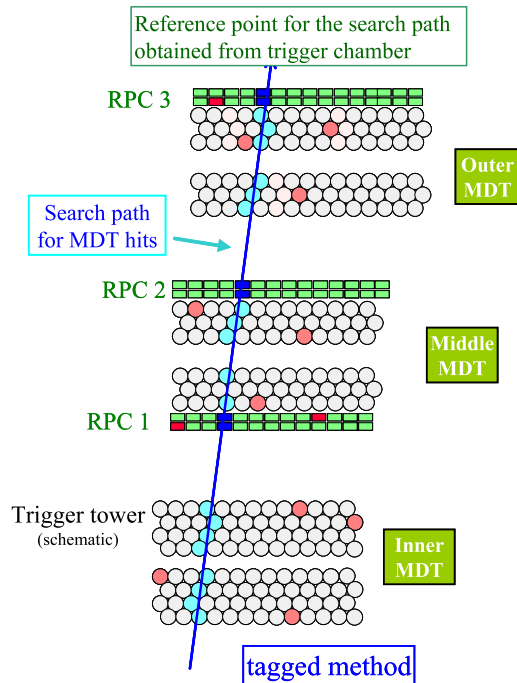

Figure 3: The tagged triggering method uses the RoI of trigger chambers in the same tower to define a search road inside which to look for hits of the candidate track. Track segments of several MDT can be combined to give a precise estimate for the p_T of the track.

To simplify the drift time measurement for the fast readout, the clock frequency of 1.28 GHz, used internally by the TDC and corresponding to a least significant bit (lsb) value of 0.78 ns, needs to be relaxed. For the fast readout a clock frequency of 80 or 160 MHz may be sufficient, corresponding to lsb values of 12.5 ns and 6.25 ns, respectively. Given the drift velocity of 37.5 ns/μm in the Small drift tubes, the corresponding RMS position errors are 135 and 68 μm. With a lever arm of about 150 mm between the sMDT multilayers, this leads to an angular RMS

resolution of 0.9 and 0.45 mrad, respectively, both values being compatible with the required angular resolution of < 1 mrad.

Two methods have been proposed for the implementation of a sMDT based L1 triggering scheme. The "tagged" method (see Fig. 3) uses the early information ("Level-0") on a candidate track (RoI), obtained from close-by trigger chambers, as a search road for track hits in a narrow corridor of the sMDTs along the track. This way most of the background hits, located outside the search road, can be safely ignored. On a Level-0 request, local processors start to search for hits in the RoI and derive the resulting tracking angle and momentum, if applicable. The tagged method requires very limited output bandwidth, as in any given trigger tower the rate of L1 candidates is very small (< 100 Hz).

The communication path between trigger and MDT chambers leads to additional latency. Timing estimates show that a latency in the range 3.2–4.5 μs is required, too long for the available latency of 2.55 μs in phase I, but well below the limit of 6.4 μs, foreseen for phase II of the LHC upgrade. A detailed discussion of this method is given in [24].
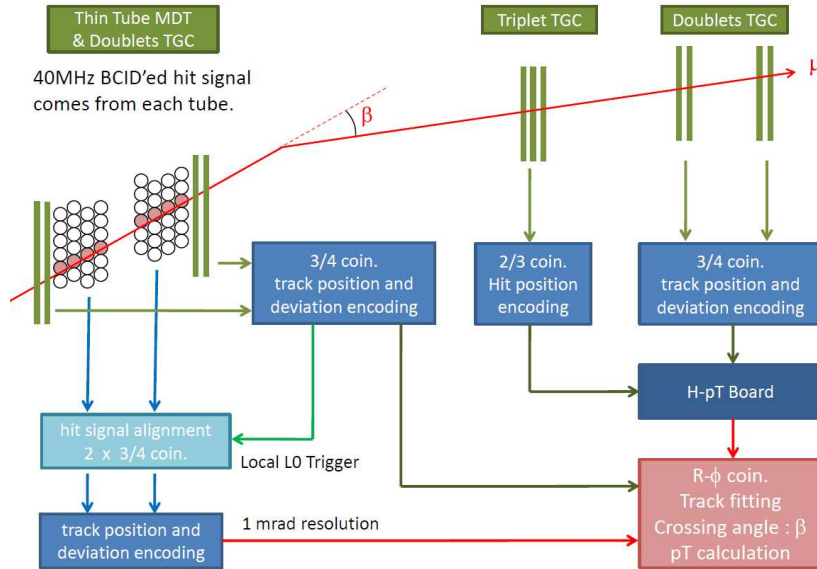

Figure 4: The untagged tagged triggering is looking for track segments in a MDT which point to the primary vertex.

The "untagged" method (see Fig. 4) uses all hits from all MDT tubes and looks for hit patterns pointing to the primary vertex. It does not make use of a preceeding Level-0 tag from the trigger chambers. Consequently, the fast MDT readout needs to transfer all incoming hits to the processors in USA15, leading to bandwidth requirements of up to about 2.5 Gbit/s per group of 24 tubes. Timing estimates for the untagged method lead to a latency of < 2.55 μs, compatible with the phase I limit by a narrow margin of 160 ns. More details about this method are given in appendix F.

In both methods the information is fed into the L1 trigger logic at the level of the sector logic (SL).

5.2 Detector technology and layout

5.2.1 Detector technology of the sTGC chambers

The structure of the new sTGC chambers is shown in Fig. 5, while the schematic layout of the proposed NSW trigger chamber system is shown in Fig. 6. This layout should be consider as one of the possible arrangements of identical small-large sectors. The 4+4-layer Small tube MDTs are sandwiched between two sTGC packages, each 5 cm thick, containing four gas-gaps each. Each gas-gap provides pad, strip and wire readout. Since the trigger chambers, unlike the MDT, do not need an overlap region for relative alignment, that part of the MDT surface is used to implement the alignment connection (purple boxes) to the projective alignment bars.
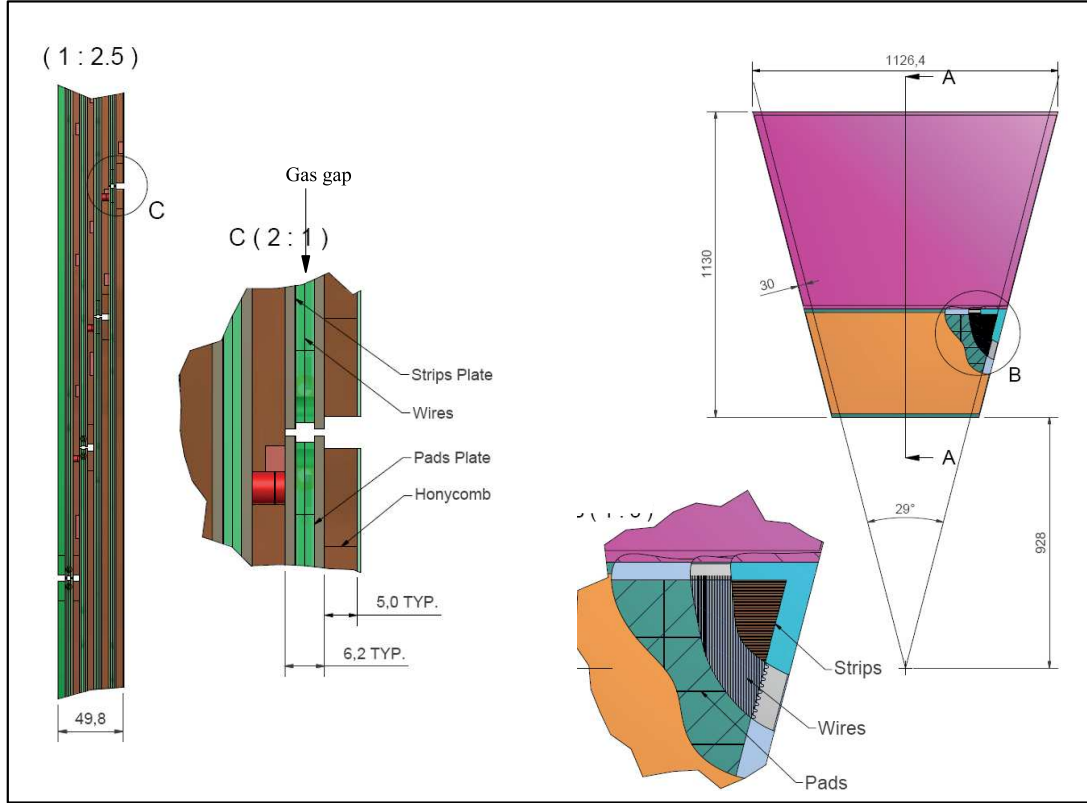

Figure 5: Schematics of the internal layout of a 4-layer TGC package, showing the pad-strip and wire readout for each gas-gap.

The internal structure of each sTGC package is the same as that shown in Fig. 5. The innermost radial sTGC packages are subdivided into two stair-like packages (to provide full coverage in 3 out of 4 layers), in order to keep short wires in the high background region. The readout of the wires is done as an OR of the segments, flagged by the corresponding pad coincidence. The preliminary dimensions of each sTGC package can be seen in Fig. 6. This corresponds to a total of 192 packages, each of them containing 4 gas-gaps, corresponding to a total of 768 gas-gaps.

The corresponding number of electronics channels is given in Table 2, where the pad surfaces increase from 7.5×7.5 cm^2 to 20×20 cm^2 at the outermost radial layers. The dimensions of

the "small", "medium" and "large" pads are determined with respect to the corresponding background rates. The pads are shifted every two layers (Fig. 7) to reduce the size of the corresponding Tower-of-Interest, which defines those strips and wires to be used for the trigger decision and readout.

The internal alignment achieved by the production of the strip patterns in the sTGC gas gap is precise to better than $50\,\mu$m, however, the transfer of this precision from gap-to-gap has only been achieved to within $150\,\mu$m. For this reason, the final precision alignment between gaps will be done using tracks from the sandwiched MDT. This requires few tracks, since the internal strip pattern within a gap is extremely precise.
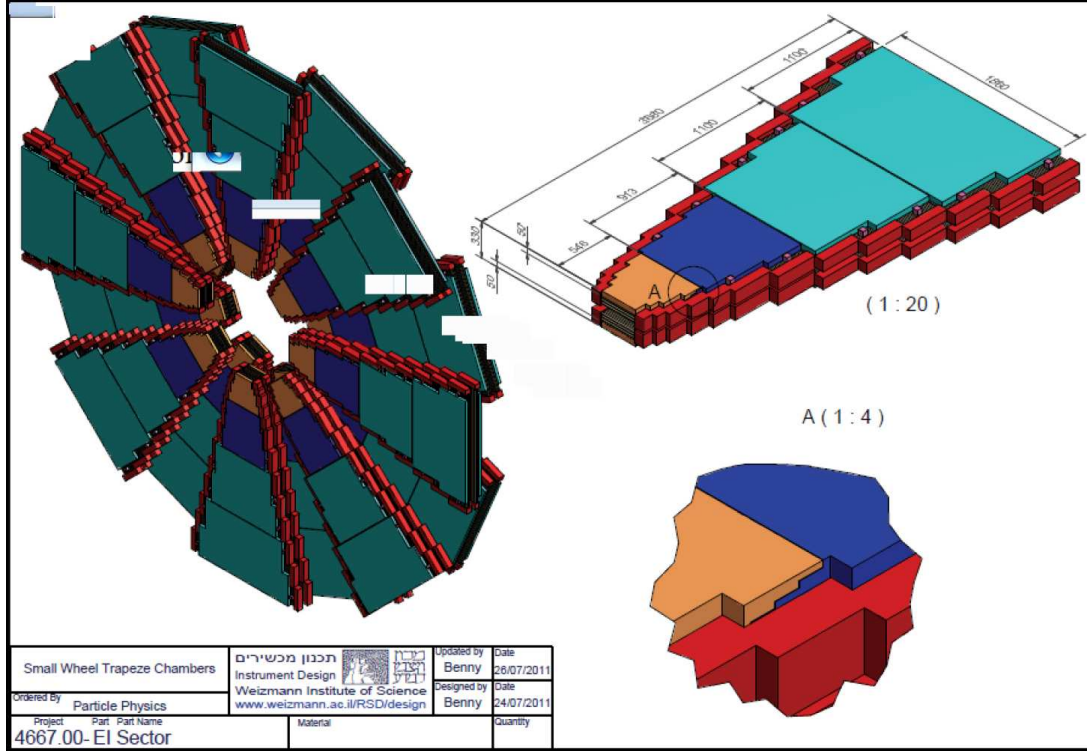

Figure 6: Schematic of the detector layout for the case of equal small-large sectors. Insert A shows the stairs-type arrangement for the innermost radial sTGC package. The purple boxes represent the alignment elements for the MDT detectors.

The mechanical stability of a TGC package is very good for vertically mounted detectors, based on ATLAS experience. The use of composite materials allows for very small sensitivity to temperature changes in the range expected for the Small Wheel. To remove any mechanical sensitivity to magnetic field in the Small Wheel region, the mounting needs to be kinematic (one fixed point, one sliding point and one plane), of the same type as presently used in ATLAS.

The processing of the sTGC signals is considerably more complex than for the existing TGCs. An accurate determination of the track position in the two chamber packages is required, and the resulting vector has to be extrapolated to the corresponding trigger sector in the Big Wheel. In this process, the trigger latency must remain below the limit defined by the present ATLAS trigger system, a limit which will also be valid for Phase I. Details of the proposed trigger and readout scheme are given in 5.4.
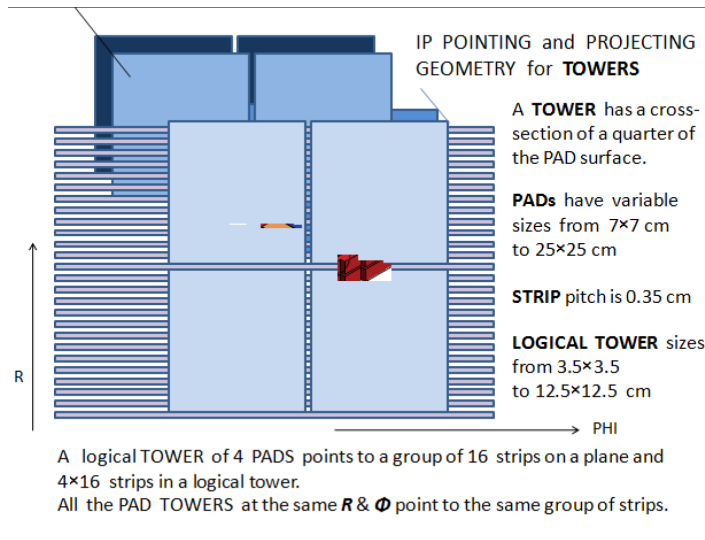
Figure 7: Schematics of Pad and strips arrangement (only 2 layers shown).

Each package will be connected to four HV lines, three LV lines and the corresponding optical fibres that transmit the trigger/data information. The HV lines will be connected to one corner of the chamber, while the LV and fibres will be connected to a trigger box, where the logic will be installed. In case of a major failure, the full TGC-MDT-TGC package will be replaced. This means that two such spare packages for each of the station types need to be constructed.

Component	Number of channels
Strips / side	135,000
Pads / side	30,000
Wires / side	27,500
For two sides detector	385,000

Table 2: Channel counts for the three readout streams for the 192 packages with 768 gas gaps.

5.2.2 Detector technology and layout of the sMDT chambers

Figure 8: Structure of the NSW (left) and 3D layout of the sMDT-sTGC chamber system (right) with the global alignment rays indicated as red tubes.

Figure 9: Layout of the integrated sMDT and sTGC chambers in the small (left) and large (right) sectors of the NSW.

The layout of the sMDT chambers for the NSWs follows exactly the present layout of the MDT chambers in the Small Wheels with fully projective small and large chamber towers in combination with the EM and EO layers. (see Figs. 8 and 9). The chamber parameters

are summarized in Table 3. There are only three radial chamber segments in each sector. The sTGC chambers are precisely positioned and kinematically mounted on the outer tube layers of the sMDT chambers on both sides. The integrated sMDT-sTGC chamber packages are connected by light rays to the global optical alignment system and with the neighbouring chambers via sensors mounted precisely on the outer tube layers of the inner multilayers of the sMDT chambers while the in-plane alignment system is integrated into the sMDT spacer structure which also carries the common chamber supports. The well understood alignment system implementation guarantees precise absolute chamber alignment from the beginning which is essential for the performance of the muon spectrometer.

sMDT chambers	EIL0	EIL1	EIL2	EIS0	EIS1	EIS2
Number of chambers	2 x 8	2 x 8	2 x 8	2 x 8	2 x 8	2 x 8
Radial extension (mm)	1095	1095	1457	1215	1276	1095
Minimum chamber width (mm)	740	1428	1968	678	1056	1434
Maximum chamber width (mm)	1380	1878	2418	1002	1380	1704
Minimum tube length (mm)	560	1248	1788	498	876	1254
Maximum tube length (mm)	1200	1698	2238	822	1200	1524
Spacer height (mm)	68	120	120	68	120	120
Thickness in z, tubes (mm)	228	228	228	228	228	228
Thickness in z, chamber (mm)	300	300	300	300	300	300
Weight/chamber (kg)	150	130	180	140	120	130
Number of tube layers	2 x 6	2 x 4	2 x 4	2 x 6	2 x 4	2 x 4
Number of tubes/layer	72	72	96	80	84	72
Number of tubes/chamber	864	576	768	960	672	576
Total number of tubes	13824	9216	12288	15360	10752	9216
Gas volume/chamber (l)	122	162	219	102	110	127

Table 3: Parameters of the sMDT chambers in the NSWs. The total number of drift tubes is 70656 and the total gas volume in each NSW 6750 l.

The design of the muon drift-tube chambers with 15 mm diameter tubes for the new Small Wheels follows as closely as possible the current ATLAS MDT chamber design in the endcap region of the muon spectrometer (Fig. 10). The chambers consist of two multilayers of four or six layers of drift tubes each in densest package. The aluminum tubes of 15 mm outer diameter and 0.4 mm wall thickness are produced according to industry standard and are chromatized for cleaning and reliable electric contact. The tubes are separated by 0.1 mm wide glue gaps during chamber assembly. The two multilayers are separated by a spacer frame carrying the supports of the integrated drift-tube and trigger chambers on the Small Wheel structure and the in-plane optical alignment system monitoring the planarity of the chambers. The aluminum spacer frame is of similar design as for the present Small Wheel MDT chambers. The main changes in the chamber design are due to the four times denser packaging of the drift tubes and their gas and electrical connections.

Central to the chamber design is the design of the drift tubes and of their endplugs (see Fig. 11). The aluminum tubes have 15 mm outer diameter and 0.4 mm wall thickness and are produced according to industry standards (DIN). The endplugs insulate the sense wire from the tube wall, center the wire in the tubes, position it with respect to the external reference surface on the endplug with an accuracy of only a few micron and provide high-voltage-safe
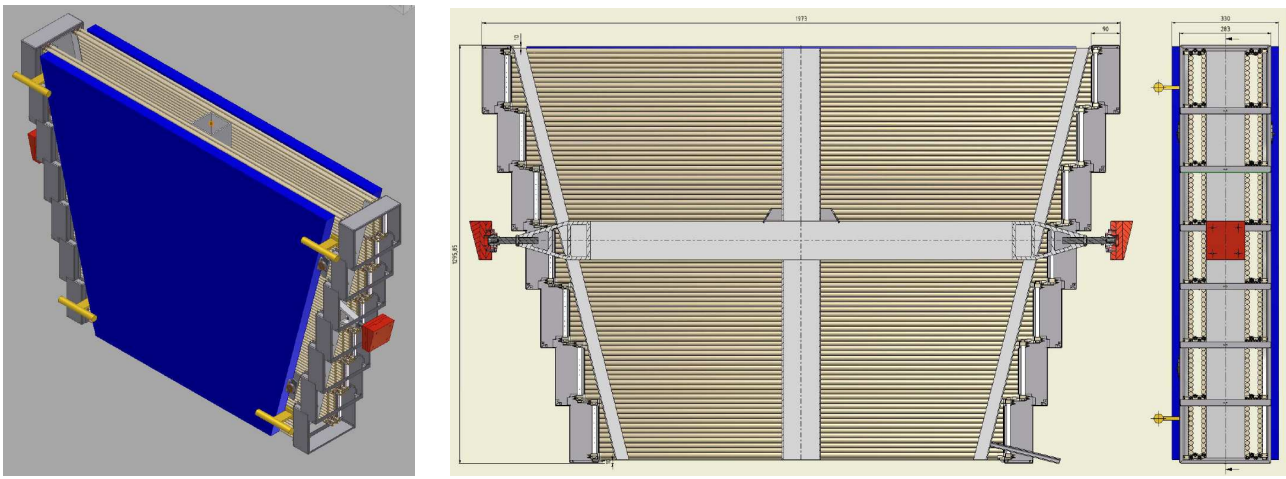
Figure 10: Small drift-tube chamber design for the new Small Wheels: 3D view (left) and cross sections in the chamber middle planes parallel and perpendicular to the tube layers (right). The mounting of the trigger chambers and of the external alignment sensor is also shown.

connections to the gas distribution manifold (see Figs. 29) and to the 24-channel readout and high-voltage interface boards ("hedgehog cards", Figs. 38).

The modular gas distribution system consists of injection moulded plastic tubes made of Pocan® without glass fiber which interconnect adjacent tubes in the direction perpedicular to the multilayer and connect them to an aluminum gas distribution bar on the readout and the high-voltage end of the multilayer.
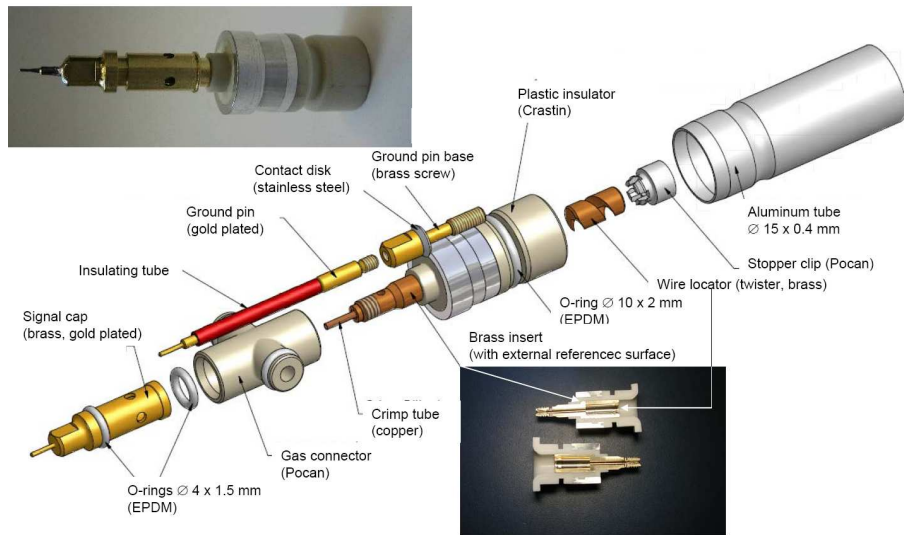

Figure 11: Exploded view of a drift tube with gas, signal and ground connections.

The readout and high-voltage supply scheme follows closely the one of the present MDT chambers using the same parameters and specifications. The high-voltage decoupling capacitors on the readout side and the terminating resistors on the high-voltage supply end are individually encapsulated in plastic containers for high-voltage protection. The plastic containers are integrated with the hedgehog cards plugged onto the gold-plated pins of the signal caps and

16

ground connectors. The ground pins are screwed into the gaps formed by three adjacent tubes In order to during chamber assembly to connect the tube walls to the ground of the hedgehog cards. This scheme allows for the high-voltage-free design of the readout hedgehog cards. Each readout hedgehog card carries a mezzanine card with the new radiation hard active readout electronics (see below). The mezzanine cards follow the shape of the hedgehog cards and are currently under development. The electronics boards are enclosed in aluminum Faraday cages which also shield the readout hedgehog cards against the mezzanine cards. The modularity of the sMDT chambers in the NSW is given in Table 5.

5.3   Performance

5.3.1   Performance of the TGC trigger chambers

The most important issue for a detector that needs to operate at high rate during a period of more than 10 years, is its ageing characteristics. For this reason, a series of small TGCs (10 × 10 cm^2) detectors were constructed and exposed to γ irradiation for various periods of time. No deterioration was observed in any of these prototypes. The one with the longest exposure was opened after a total irradiation of 6 Cb/cm of wire (i.e. 33 Cb/cm^2). Fig. 12 shows the rate and current behavior of the detector during the irradiation. No noticeable degradation is observed after the MIP dose equivalent to 2,000 days of operation at the hottest location in the ATLAS Small Wheel.
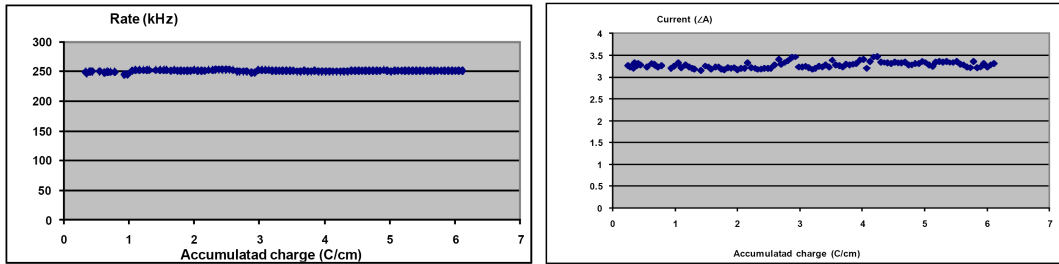

Figure 12: Counting rate and current as a function of the integrated charged in the detector.

The irradiated detector was opened to see the effect of the irradiation. Fig. 13 shows a microscope picture of a wire in the irradiated region, as well as in the non-irradiated region. The deposits in the irradiated region were analyzed, the deposits being mainly Carbon and Oxygen, as expected from the gas composition.
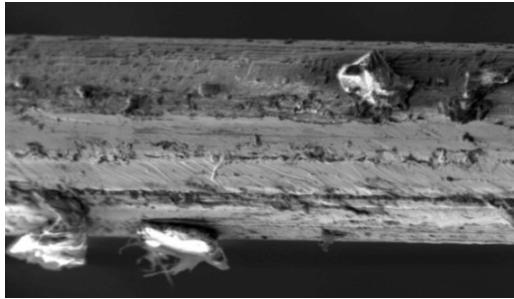

Figure 13: Deposits observed in the irradiated (left) and non-irradiated region of a wire.

In order to perform the R&D needed for the use of TGC's in the ATLAS Small Wheels, six large (ranging from 120×100 cm^2 to 70×40 cm^2) packages of TGCs, each one containing four gas-gaps, each gap with pads-strips and wire readout, have been constructed. These detectors were irradiated in various facilities to evaluate their behavior and position resolution. The time, position and angular resolutions were determined from measurements performed in the H8 facility at CERN, while the efficiency for MIPs under a high full area irradiation with γ' s was performed at the SOREQ Nuclear Center (Israel) using ^{6}0Co source, while triggering on cosmic muons.

The sensitivity to neutrons was measured at the Demokritos Nuclear Center (Greece). To simulate the present proposal, the trigger used at the H8 test-beam was the expected 3-out-of-4 coincidence of pads. The time resolution of this trigger with respect to a beam-defined scintillator is shown in units of 0.8 ns in Fig. 14 (left). It can be seen that the time resolution of the system is able to provide the bunch crossing identification with high efficiency.
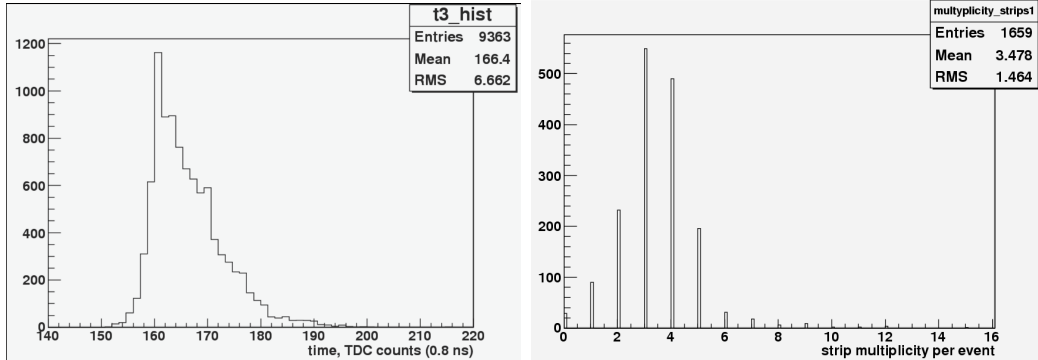

Figure 14: Left: Time difference between 3-out-of-4 pad trigger with respect to the beam scintillator in units of 0.8 ns. The FWHM is 11 ns. 99% of the distribution is within 25 ns. Right: Strip multiplicity for a MIP on a typical gas gap.

Fig. 15 shows the individual efficiencies of each of the layers for Pads, Strips and wires of one such package, using the Time-over-Threshold method. It can be see that they are all fully efficient at an operating voltage of 2.9 kV, which was used for the rest of the tests.

The position resolution of each individual gap was measured by using clean muon tracks in the small tube MDT test detector that was part of the test beam set-up. The strip multiplicity distribution that provides the charge centroid is shown in Fig. 14 (right).
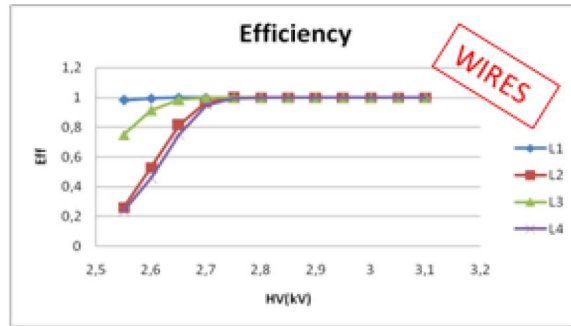

Figure 15: Plateau curve for each of the gaps used in the test, using the T-O-T method.

The TGC position resolution was calculated from a fit to the difference between the measured position in a given layer and the position extrapolated from a fit to the other three layers, as shown in Table 4 (before and after the correction for inter-gap misalignment). A typical distribution for one layer is shown in Fig. 16. It can be concluded that the position resolution achieved with the TGC layers fulfills the requirements for the NSW and provides a valuable complement to the position measurements of the MDT.

The position resolution as a function of incident angle has been measured in the past using a regular ADC to determine the charge in each individual strip. This measurement will be

19

repeated in the August 2011 test beam using Time-over-Threshold. The dependence of the single layer resolution as a function of angle is shown in Fig. 17.

Layer	$\sigma_{corr}(\sigma_{nocorr}) \pm \Delta\sigma[\mu\mathrm{m}]$
1	66.2 (120.9) ± 1.2
2	66.7 (79.8) ± 1.1
3	63.6 (76.0) ± 1.0
4	63.8 (116.49) ± 1.0

Table 4: Position resolution in the 4 layers after (before) correcting for individual layer position.

The angular resolution of a single sTGC package was obtained by comparing the angle between one package of sTGC's (four gas gaps) with the one measured with the Small Tube MDT test chamber. The difference has a resolution of 3 mrad. Having such a resolution with a single sTGC package (5 cm thick) implies that with two packages separated by 300 mm, the angular resolution of the system would be better than 0.3 mrad at the Level-1 trigger.

The measured single layer efficiencies for MIP's in a γ background has been measured by triggering with cosmics under a high irradiation flux. The results are shown in Fig. 18, left. Similarly, this was done with 5.5 MeV neutrons. The corresponding single layer efficiency is shown in Fig. 18, right.
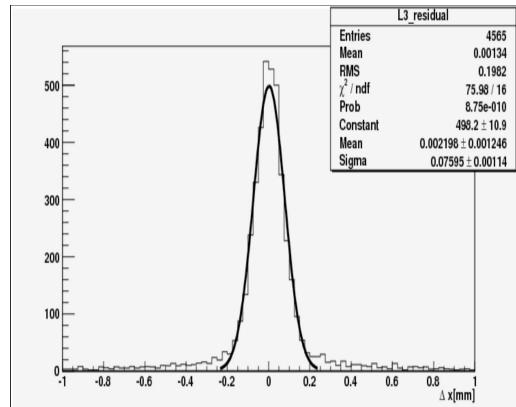

Figure 16: Typical residual for one of the layers with respect to the fitted line.

Figure 17: Resolution vs. incident angle as measured with muons in H8.

Finally, by using the Time-over-Threshold method, one can reject single gas-gaps measurements, polluted by a δ-ray, a γ or a neutron-conversion, by demanding less than six strips in a
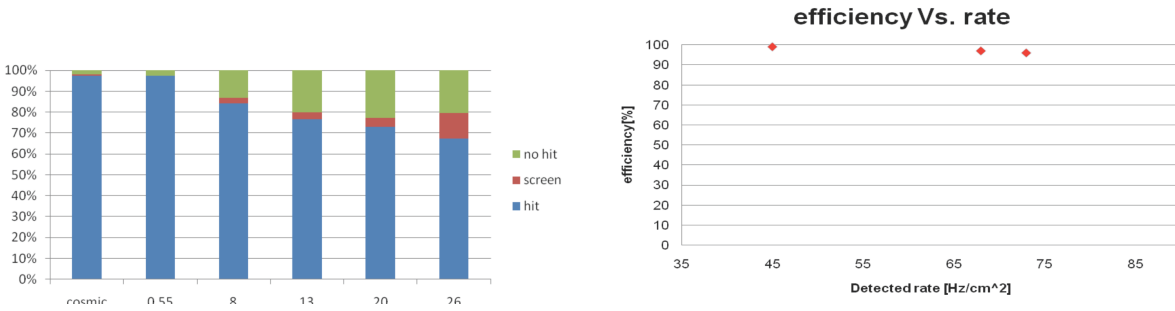
Figure 18: Left: Single layer efficiency in kHz/cm² on a large chamber under uniform γ-irradiation (strip length= 1.2 m). Right: Single layer efficiency for MIPs under 5.5 MeV neutron irradiation.

cluster and a cut on the ToT. This is illustrated in Fig. 19, where one can see the passage of a muon through the four gas-gaps, (a) without contamination, (b) with a δ-ray in layer one and (c) with a neutron impinging in layer three.
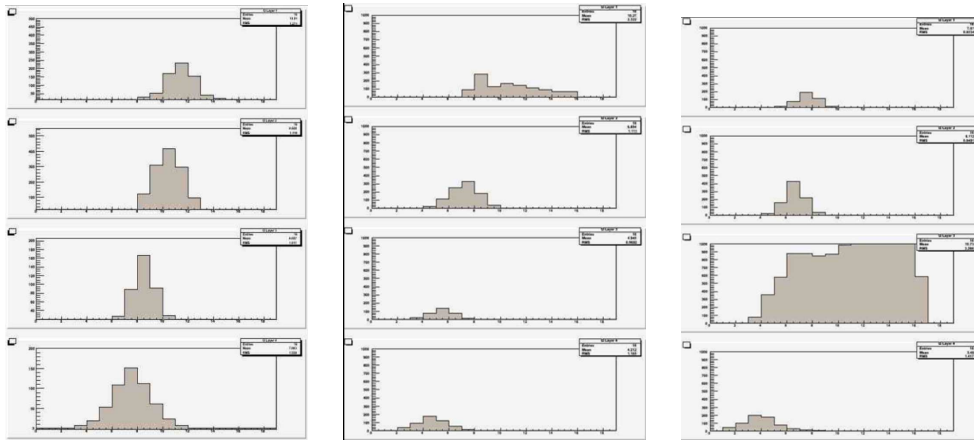

Figure 19: Event display of a) a clean muon track, b) a muon track with a δ-ray in the first gas-gaps and c) a neutron interacting in the third gas gap. The unit of the horizontal axis is 25 ns/division.

5.3.2 Performance of the sMDT tracking chambers

In order to verify the performance of the 15 mm diameter ("small") drift tube chambers, extensive tests of the full-scale prototype chamber with 15 mm diameter drift tubes have been performed in the H8 high-energy muon beam in 2010 and 2011 together with integrated TGC chambers (see Fig. 39, left) and, using cosmic ray muon tracks, in the CERN Gamma Irradiation Facility (GIF) with a 500 GBq ^{137}Cs source (Fig. 39, right). The standard ATLAS MDT readout electronics has been used with the adjustable deadtime set to the minimum value corresponding to an overall effective deadtime of 200 ns. The spatial resolution and efficiency of the individual drift tubes and of the whole chamber have been measured for different γ irradiation rates where the individual drift tubes have been illuminated uniformly over the whole length.

As a measure for evaluating the tracking efficiency, we define the "3σ-efficiency" as the probability of detecting a tube hit within a distance from the muon track of 3 times the drift tube resolution σ, where the muon track is defined by the other tubes on the track and extrapolated to the active volume of the tube. Similarly, the drift tube resolution as a function of the drift radius is determined by an iterative method excluding the evaluated tube from the track reconstruction in the chamber [22].
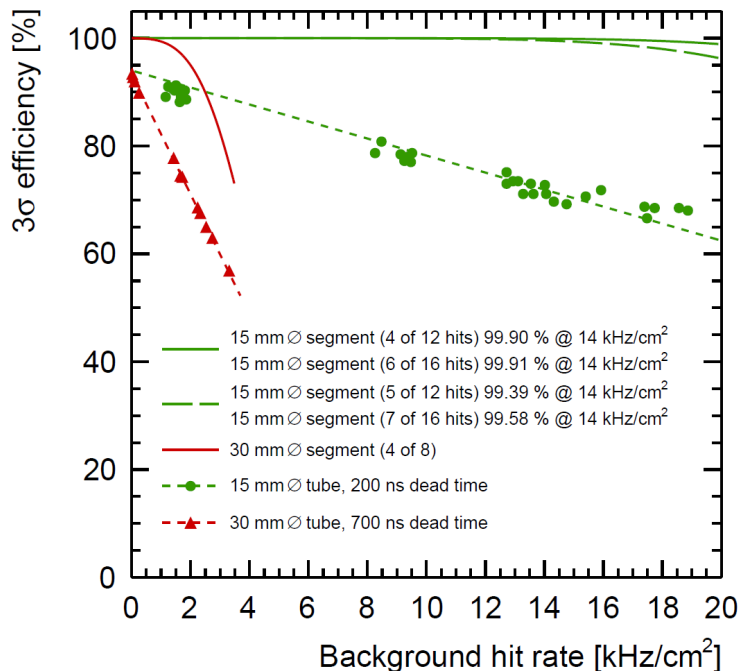

Figure 20: The 3σ efficiency of individual drift tubes of 0.5 m length (as at the inner bore of the Small Wheels) as measured at the GIF as a function of the background hit rate. Results for 15 mm and 30 mm diameter tubes are compared. The corresponding calculated track segment reconstruction efficiencies in 2 x 4 layer MDT chambers and in sMDT chambers with 2 x 6 or, optionally, 2 x 8 tube layers are also shown.

Fig. 20 shows the average 3-σ efficiency of 15 mm diameter drift tubes and the track segment reconstruction efficiency of the prototype chamber as a function of the γ background flux in comparison with the results for the 30 mm diameter tubes from previous tests of a BOS MDT chamber in GIF [12], [13]. At low background rate, the 3σ tube efficiency of 30 and 15 mm

22

diameter tubes is 94%. The efficiency loss is due to δ-rays created by interactions of the muons in the tube walls which produce hits earlier than the muons. The degradation of the efficiency with increasing rate follows the predicted behaviour. The redundancy of track measurements in the different drift tube layers is sufficient to achieve more than 99% track segment reconstruction efficiency up to the highest background rates.
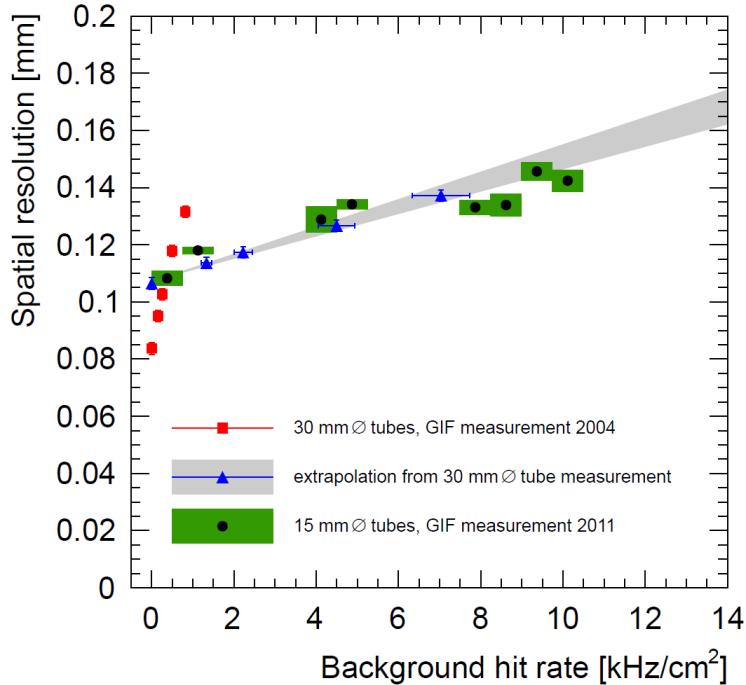
F

Figure 21: Dependence of the *average* drift tube resolution (with time-slewing corrections) on the background hit rate. The measurements for 30 mm and 15 mm diameter drift tubes at the GIF are compared.

ig. 21 shows the dependence of the average 30 mm and 15 mm diameter drift tube resolution (taking into account time slewing corrections) on the background hit rate measured at the GIF. The measurements confirm the expectation that the degradation rate of the spatial resolution with the background flux is reduced by a factor of 10 for 15 mm compared to 30 mm diameter tubes (see the discussion in the Appendix).

At low background rates, the average resolutions of 15 and 30 mm diameter drift tubes at low background rates have been measured to be $110 \pm 2\,\mu$m and $83 \pm 2\,\mu$m, respectively. At the maximum background hit rate of 10 kHz/cm^2 at which the GIF measurements could be performed, the average 15 mm diameter drift tube resolution is 143 ± 4 μm. At 14 kHz/cm^2 rate it will still be better than 170 μm.

5.4   sTGC Level-1 trigger and readout electronics

The strip signals in the sTGC of the NSW are used to extrapolate tracks to the Big Wheel where they are corroborated by the Sector Logic with the existing 2-out-of-3 and 3-out-of-4 coincidences in the Big Wheel chambers. The fine granularity of the extrapolation results in high efficiency for trigger rejection. The electronics added to accomplish this must not cause the latency to the Sector Logic to exceed the existing $1.05\,\mu$s. A detailed breakdown of the sTGC trigger latency is given in the appendix (C.1).

The sub-sector in the Big Wheel trigger station of the extrapolated muon is found as follows: In the two sTGC packages of the NSW, a local trigger is made from two sets of 3-out-of-4 pad coincidences, corresponding to a tower of four pads in each of the two quadruplets. Pads in alternating layers are shifted by half a pad in both dimensions to give a 4-times higher granularity of logical towers. The triggering tower selects the strips in its region for transmission to eight centroid finders, one for each layer. This selection leads to a 20-fold reduction in the number of strips to be processed as well as in the number of centroid finders. The four centroids in each sTGC package are averaged to give two points in 3-D space, defining a vector which points to a sub-sector in η, ϕ of the Big Wheel. The $\sim$60 μm resolution together with their distance of 250 mm provides an angular accuracy of better than 0.4 mrad.

A simple block diagram of the trigger processing chain is shown in Fig. 42. Its elements are elaborated below. The trigger functionality is split between on- and off-chamber locations. Two architectural options are discussed. A more detailed block diagram of the sTGC trigger logic for two quadruplets is shown in appendix (C.1) as part the description of a trigger demonstrator. In order to measure the trigger latency for a realistic FPGA design, a demonstrator has been implemented with a commercial FPGA evaluation board.

ASD: The baseline is to use BNL's VMM Front End chip, now under development. The planned analog parameters of this chip, 0.11 to 2.0 pC input charge range, 20-25 ns peaking time, and time-over-threshold discriminator, match the needs of the sTGC detectors. The first prototype chips will be available early in 2012. The sTGC version of this ASD has LVDS discriminator outputs suitable for the Time-over-Threshold trigger logic.

Pad tower trigger: The Pad tower trigger, whose logic is described above, is on-chamber and implemented in radiation tolerant electronics. The coincidence tags a bunch crossing and the group of strips passing through the triggered tower in each layer that must be selected for processing by the Selector.

Selector: From the pad tower trigger, the Selector receives the Id of one of about 20 groups of 16 strips that must be routed off-chamber for further processing.

Time-over-Threshold converter: This module measures the time between the rising and falling edges of the ASD Time-over-Threshold level in steps of 1 ns and with a 7-bit dynamic range. This time is approximately in proportion to the charge on each strip. Optimized parameters will depend on the final ASD characteristics. The converter is fairly simple. The demonstrator implementation uses a 1-to-10 serial-to-parallel converter and logic running at $1/10^{th}$ the sampling clock speed to count the time between edges.

Centroid finder and averager: The centroid finder currently calculates the centroid from

the charge on up to five strips. Centroids are included in the average only if the number of strips above threshold is below a certain maximum value in order to exclude δ-rays and conversions (see Fig. 19). It is expected to implement this logic off-chamber in reprogrammable FPGAs.

Extrapolator: The extrapolation of the track vector to the Big Wheel is done using Look-up-Tables (LUTs) for both the R and ϕ coordinate. The LUT inputs for a given R are the centroid average, the radius and the difference in the centroid averages of the two quadruplets. The LUT input for ϕ is the triggering pad tower ID.

We seek to minimize the amount of on-chamber electronics, because access and power are very limited for the Small Wheel, and on-chamber electronics must be radiation tolerant. Radiation tolerant ASIC's are likely required on-chamber even though reprogrammable FPGAs would be more flexible. Radiation tolerant FPGA's are possible for locations away from the Small Wheels.

Two architectural options for the Selector and Time-over-Threshold to digital converter are shown. One option requires more complex radiation tolerant electronics, but can handle multiple triggers; the other option requires higher bandwidth links. The two options, detailed below, are:

Option A: Time-over-Threshold converter per channel, either in, or behind the ASD, but BEFORE the Selector: Here, on every beam crossing, the Selector selects 20 strip ToT's per layer (7-bits each) indicated by the pad tower coincidence. The needed link bandwidth to the off-chamber Centroid Finder (including ToT's, BCID, R and ϕ IDs, parity) is $140 + 20 = 160$ bits at $40\,\text{MHz} = 6.4\,\text{Gb/s}$.

Option B: Time-over-Threshold AFTER the Selector: Here, the ToT converter can be off-chamber with the Centroid Finder; also fewer ToT converters are needed. The needed link bandwidth from the Selector to the off-chamber TOT converter is: 20 channels at $1\,\text{Gb/sec}$ per channel $= 20\,\text{Gb/sec}$ for the expected maximum ASD pulse width of $100\,\text{ns}$.

The disadvantage of Option A is the increase in complexity and amount of on-chamber radiation tolerant electronics. The ToT converters are not overly complex, resembling simple deserializers, but on-chamber radiation tolerant ASICs are none-the-less higher risk than off-chamber FPGAs.

The disadvantage of Option B becomes clear when the background is high enough that another pad tower trigger occurs in one of the 19 non-selected groups of strips during the $100\,\text{nsec}$ of the TOT conversion. Such triggers will be lost since both the selector and ToT converter are busy until the end of the $100\,\text{nsec}$ maximum pulse duration. One can increase the complexity of the selector and route subsequently triggered strips in a round-robin fashion to additional TOT modules after the selector. This increased complexity of the radiation tolerant selector probably eliminates any advantage of this option. Option A on the other hand can handle a pad tower trigger anywhere every $25\,\text{nsec}$.

The choice between the options depends on reliable background estimates and details of radiation tolerant ASICs and of serializer speeds and power, all of which are not sufficiently known at this time.

Further details of the sTGC Level-1 trigger and readout electronics can be found in appendix (C.1).

Latency (calculation, measurement with demonstrator)

A detailed discussion of the latency expected for the sTGC readout is presented in the appendix (C.1).

Compatibility with Phase II upgrade

The pipelines and derandomizers will be designed to handle a $500\,\text{kHz}$ Level-1 trigger rate and to accommodate up to $10\,\mu\text{s}$ Level-1 latency.

Time schedule for the sTGC electronics development

The schedule for prototyping, development and production of the sTGC trigger electronics is given in the appendix C.3, Table 17.

5.5 Readout Electronics of the sMDT Chambers

The readout of the Small MDT tubes will follow the proven architecture of the present MDT system. A number of additions and modifications, however, will be necessary in order to adapt the rate capability of the readout chain to the requirements of the SLHC. For the mechanical integration of the readout electronics with the Small tube chambers, the layout of the electronics will have to be adapted to the four times higher tube density at the ends of the chambers. Finally, the radiation tolerance of all components will have to comply with the high radiation levels, in particular at the inner boundary of the Small Wheel.

5.5.1 Architecture of the present MDT chamber readout

In the present readout scheme tube signals are routed via a PCB ("hedgehog card") to a piggy-back card ("mezzanine card"), containing an Amplifier and Shaper, followed by a Discriminator with adjustable threshold, all three functions being integrated in a radiation tolerant ASIC (ASD). The discriminator outputs, in turn, are routed to a TDC, where each leading and trailing edge signal receives a high-precision time stamp, which is retained, together with the corresponding channel number, in a large internal buffer of the TDC ("Level-1 buffer").
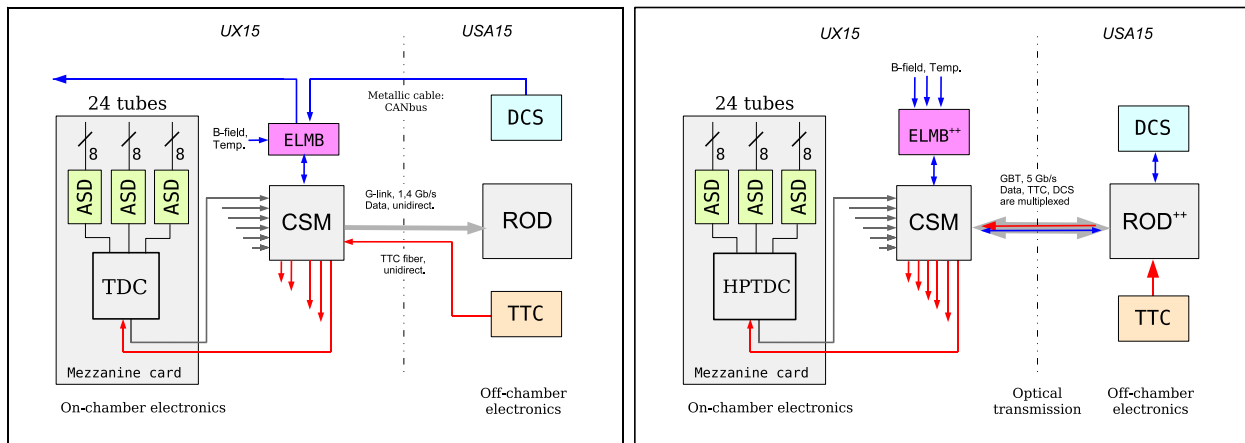

Figure 22: Schematic diagram of the present (left) and of the future MDT readout chain (right). Using the GBT in the new readout scheme improves the readout bandwidth and simplifies logistics, as TTC, Data readout and DCS are transferred over the same bi-directional link. The omission of CANbus cabling due to GBT will reduce the risk of ground loops between chambers and improve system reliability.

When the TDC receives a Level-1 trigger, a subset of the recorded hits, corresponding to a pre-defined time window, are retained for readout and are forwarded to the data concentrator of this chamber, the "Chamber Service Module" (CSM). From there, data are sent to the off-chamber electronics in USA15, the "Readout Driver" (ROD). A CSM can serve up to 18 mezzanine cards. The operation parameters of the analog frontend (ASD) and the TDC are controlled by a JTAG string, which is distributed by the Detector Control System (DCS) to the CSM, which sends it individually to each mezzanine card. Fig. 22 gives the layout of the present system. A detailed presentation of the MDT readout electronics is given in [5]. The ASD and TDC ASICs are described in [7] and [8].

5.5.2 Architecture of the sMDT chamber readout

For the evolution of this architecture into matching the requirements of the Small tube readout, a number of problems limiting the performance of the present scheme has to be overcome. Given the high rate capability of the Small MDT tubes, the bandwidth of the readout system has to be increased. Due to the limitations of the internal buffering scheme and processing speed, the present TDC can only handle average tube rates up to about 300 kHz per tube without losing data, while tubes in the NSW would run up to 1200 kHz (Table 1). An improved TDC is therefore an essential requirement for a new readout design.

Another limitation of the readout bandwidth comes from the optical link, connecting the CSM to the ROD, which only provides a usable bandwidth of 1,4 Gbit/s. Fig. 23 shows occupancy and efficiency of Large and Small tubes as a function of tube hit rate.
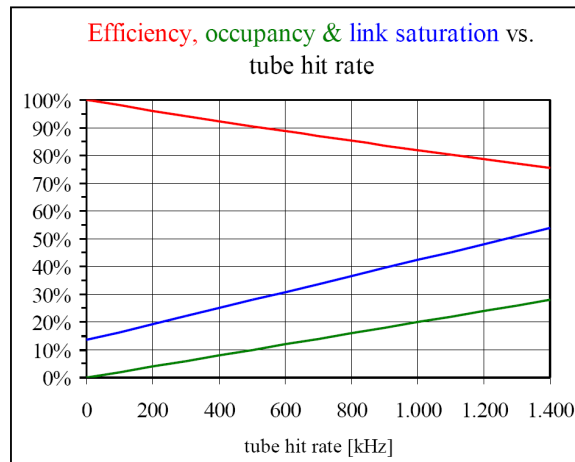

Figure 23: Green: Occupancy as a function of tube hit rate, assuming a dead time of 200 ns (equal to the maximum drift time) after each hit. Red: Resulting efficiency with 200 ns dead time. Blue: Saturation of the mezzanine-to-CSM link at 100 kHz L1 trigger rate. The load of 15% at zero hit rate is due to overheads in the transfer protocol.

The technologies used for the existing ASICs in the MDT readout are no more available from industry, and the following new components have therefore to be introduced into the new readout system.

(a) The ASD is re-designed in the IBM 130 nm technology. A 4-channel prototype, demonstrating the analog parameters, has already been produced and works correctly. Most analog parameters of the previous design are preserved. A full 4-channel prototype chip including the digital part (see Fig. 24) has been delivered in September 2011 and is under test. The final step in the ASD chip design is the extension to 8 channels.

(b) The TDC will be replaced by the HPTDC, designed by the CERN-MIC group ([6]). This 32-channel device has an improved internal buffering scheme as well as higher transfer and processing speeds. If only 24 out of the available 32 channels are used, the unused channels can be disabled to save power.

(c) The CSM collects data from a MDT chamber, formats the event and sends data, trigger-by-trigger, via an optical link to the ROD in USA15. All logical operations are performed by an FPGA, which will need to be upgraded to higher radiation tolerance. While the present CSM serves up to 18 mezzanine cards, the new CSM will have to serve up to 24 cards.

(d) The link connecting the CSM to the ROD will be replaced by a GigaBit Transmitter link (GBT), developed by CERN. This link provides a 3 times higher transfer rate (Gbit/s), compared to the presently used S-link [9].

(d) The readout of voltages and temperatures on the mezzanine cards will be done via the DCS channel of the GBT. To collect ADC readings from temperature sensors on the chamber and from B-field probes, a new version of the ELMB will be used. Aim would be to interface this new device ("ELMB++") directly to the CSM, so these data could be read out through the DCS channel of the GBT. This way, the presently used CANbus cabling could be omitted, simplifying installation and reducing the risk of ground loops.

Figure 24: The new 4-channel ASD chip with full analog and digital functionality on the test board.

Chamb. type	Tubes× layers×MLs	Tubes/ chamber	Tubes total	Mezz.cards/ chamber	Mezz.cards total	CSMs/ chamber	CSMs total
EIL0	$72 \times 6 \times 2$	864	13824	36	576	2	32
EIL1	$72 \times 4 \times 2$	576	9216	24	384	1	16
EIL2	$96 \times 4 \times 2$	768	12288	32	512	2	32
EIS0	$80 \times 6 \times 2$	960	15360	40	640	2	32
EIS1	$84 \times 4 \times 2$	672	10752	28	448	2	32
EIS2	$72 \times 4 \times 2$	576	9216	24	384	1	16
Total side A + C:			70656		2944		160

Table 5: Electronics channels (drift tubes) and readout boards in the NSW. Each mezzanine card serves 24 drift tubes, matching the modularity of the chambers with 6 and 4 tube layers per multilayer. Each CSM serves up to 24 mezzanine cards. Chambers with more than 24 mezzanine cards are served by two CSMs.

Another stringent requirement for the realization of the new readout scheme is the mechanical integration of the on-chamber readout electronics with the chamber mechanics, as the density of channels at the tube ends is four times higher than in the case of the 30 mm tubes. The following design changes will therefore be implemented.

(a) HV decoupling capacitors are located in 15 mm diameter cylinders at the tube ends, see Fig. 38. The density of signal routing on hedgehog cards is thus no longer limited by insulation distances between HV and ground or signal traces on the PCB.

(b) To match the higher tube density, the space on the mezzanine card has to be used more efficiently. For this purpose, the passive protection circuitry of the ASD inputs will be moved to the hedgehog card.

(c) For the interconnection between mezzanine cards and new CSM, we foresee to use the same 40-wire cables as was used in the present system. Its moderate diameter and high flexibility may be important for fitting the new MDTs into the limited space in the Small Wheel.

The modularity of the readout system of the Small tube sMDTs for the NSW is given in Table 5.

Power consumption of the electronics

While the power consumption of the on-chamber frontend electronics of the present system is about 30–40 W/chamber ([5], table 3), the consumption will now be about 2.5 times as high, due to tube density and increased consumption of TDC, optical link and other component.

Chamber type	mezz.s/ chamber	current/ mezzan.	current/ CSM	current/ chamber	power/ chamber at 3.3 V	power/ chamber at 4.5 V
		A	A	A	W	W
EIL0	36	18	3	21	69.3	94,5
EIL1	24	12	1.5	14	44.6	60.8
EIL2	32	16	3	19	62.7	85,5
EIS0	40	20	3	23	75.9	103.5
EIS1	28	14	3	17	56.1	76.5
EIS2	24	12	1.5	14	44.6	60.8
Power per Large + Small sector [W]					353	482
Power per side [W]					2825	3852

Table 6: Power requirements for the readout electronics of the NSW. Each mezzanine card consumes about 0.5 A, each CSM about 1.5 A at 3.3 V. The voltage delivered to the CSM is assumed to be 4.5 V, the voltage difference being consumed in local voltage regulators.

A detailed breakdown of the expected power consumption of the MDT chambers in the NSW is presented in Table 6. The total power consumption of 8.4 kW is less than the consumption

of the presently installed CSC (11.5 kW, see [2], Table 46). Yet, the removal of the heat may require flushing with dry air, as significant temperature gradients may influence the spatial resolution of the MDT and natural air convection is obstructed by the tight space constraints in the high-η region of the Small Wheel.

5.6   Services, infrastructure and DCS

1. *Description of service scheme (including power system, read-out, trigger, alignment), cooling needs and other special requirements*

2. *Table with number of services (number of cables, outer diameter, cross section of leads)*

3. *Table with power consumption (per channel, chamber, total)*

4. *Required rack space*

    (a) *UX15 (include maximum allowed distance to detector if any)*

    (b) *US15 (power system)*

    (c) *USA15 (DAQ)*

5. *Gas system and distribution*
   Details on number of gas manifolds per sector (include drawings) and connections to chambers (serial, parallel?)). Size of pipes
   Required nominal, minimum, and maximum flow
   Required precision of gas mixture
   Safety measures in case of inflammable gas
   Required rack space for gas system in SGX1, USA15, UX15

6. *Integration in DCS system, requirements for DCS*

Gas system and distribution   The gas system is a natural extension of the present TGC gas system, which will be extended from the present eight manifolds (four for EIL4 TGCs and four for the SW TGC chambers) to one containing 20 manifolds (four for the EIL4 chambers and 16 for the new Small Wheel chambers (one/layer for the upper and similarly for the lower chambers). This will be less than the normal manifolds in the Big-Wheels and can be easily be added to the present SW racks. The manifolds will be running at a flow rate of 40l/hr of the regular TGC gas mixture, which corresponds to a volume exchange every four hrs. The extra flow corresponds to a 25% increase to the present TGC gas flow, which can be implemented in the present gas system, without any additional modifications, except the extra flowmeters in the present SW racks. The safety system for the new detectors will be the same as for the present one, that were approved by TIS.

Integration in DCS system, requirements for DCS

- Chamber charge monitor

Cable	Number of cables (granularity)	Outer cable diam. (mm)	Cross section of leads (mm^2))
HV			
LV			
Monitoring and control			
Front-end links			
Calibration			
Alignment			
Miscellaneous			

Table 7: Example table number of services per chamber

Chamber	Number of channels	Power consumption per channel	Total power consumption

Table 8: Example table: Number and types of chambers per sector

- HV control and monitoring, trip recovery

- LV power control and monitoring

- Temperature monitoring

- Link health statistics

- ASD configuration parameters (threshold, peaking time, etc.)

- Front End trigger and readout configuration parameters (delays, channel masks, pipeline depth, etc.)

6 Expected muon performance with NSW [SV]

Discussion of overall performance. L1 trigger, muon reconstruction, efficiency, fake, sensitivity to a few layout parameters (number of layers, ...),

7 Integration, assembly and commmissioning [JD]

8 Cost, resources and schedule [LP, TK]

9 Conclusions

Appendices

A   Radiation background

Discussion of expected cavern background and its uncertainty based on simulations and measurements with muon detectors, and finally give a reference figures and safety factor.

- *Overview of cavern background. It's nature, origin, shielding strategy*

- *Simulation result. R distribution in the small wheel region. 14 TeV, Al beam pipe, 14 TeV steel beam pipe, 7 TeV steel beam pipe.*

- *Measuremenents with pp collision. MDT, CSC*

- *Summary figure. Reference figures.*

A.1   simulation

B   Small-Diameter Muon Drift Tube Detectors

B.1   Tracking in a high–background environment

In order to study the performance of the MDT chambers at high background rates, a full-scale ATLAS BOS chamber has been extensively tested in the CERN Gamma Irradiation Facility (GIF) [12, 13]. The results showed that the drift-tube chambers provide efficient and high-resolution tracking in combination with fast trigger and second-coordinate chambers up to very high occupancies above 20 % [20] which will be reached in the ATLAS endcap muon spectrometer already at twice the LHC design luminosity.

Reduction of the outer drift-tube diameter from 30 mm in the present ATLAS Monitored Drift Tube (MDT) chambers to 15 mm while keeping the other parameters, including the gas gain of $2 \cdot 10^4$, the sense wire diameter of 50 μm and the tube wall thickness of 0.4 mm unchanged leads to a significant improvement of the rate capability of the drift-tube chambers which is more than sufficient for their operation in the new Small Wheels at the highest background rates expected for LHC luminosity upgrades in the forward regions of the ATLAS muon spectrometer.
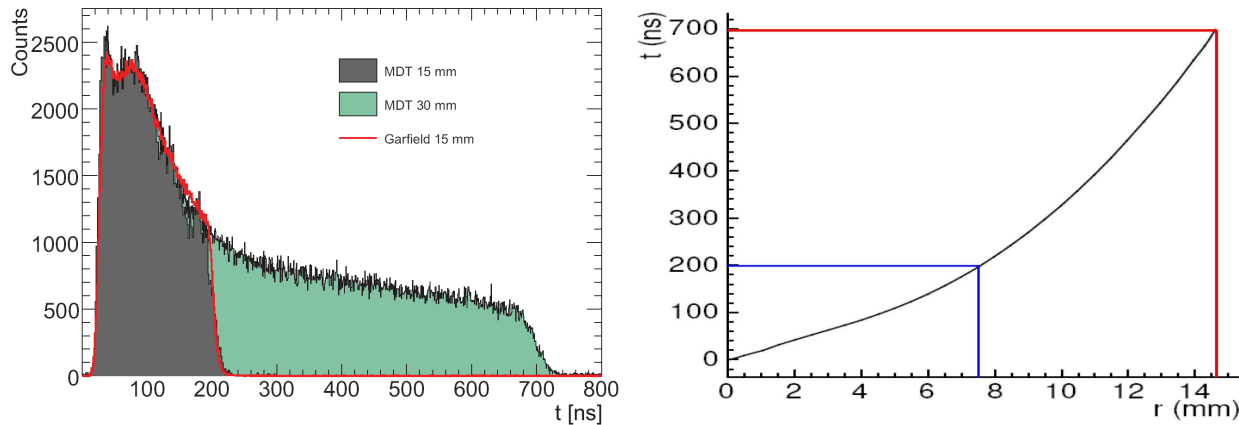

Figure 25: Drift time spectrum (left) and space-to-drifttime (r-t) relationship (right) of circular drift tubes of 30 mm and 15 mm diameter operated with Ar:CO$_2$ (93:7) gas mixture at 3 bar and gas gain of 20000. The Garfield simulation [16] of the drift time spectrum of 15 mm tubes is overlaid.

The standard MDT operating parameters are kept for the small-diameter drift tubes (see Table. 9). With the MDT gas mixture of Ar:CO$_2$ (93:7) at 3 bar absolute pressure, the gas gain of $2 \cdot 10^4$ is achieved at an operating voltage of 2730 V for 15 mm diameter drift tubes. Under these conditions, the maximum drift time is reduced by a factor of 3.8 from about 700 ns to 185 ns by shrinking the tube diameter by a factor of two (see Fig. 25, left) [15]. In addition, the background flux hitting a tube is reduced by a factor of two. Altogether, the drift-tube occupancy is reduced by a factor of 7.6. 2 x 6 drift-tube layers at radii $R < 220$ cm in the Small Wheels and 2 x 4 layers at larger radii are sufficient to provide very robust tracking with track segment reconstruction efficiencies of better than 99 % up to the highest expected background rates (see details of the chamber performance below).

The space-charge distribution caused by the ion clouds drifting towards the tube wall during

a particle crossing modifies the local electric field, influencing both the drift velocity and the gas gain. By lowering the effective potential experienced by the electrons drifting towards the wire, high background flux leads to decreasing gas gain. The resulting signal loss grows with the inner tube radius r_2 proportional to $r_2^3 \cdot \ln(r_2/r_1)$ [17], where $r_1 = 25$ μm is the wire radius, and therefore is 8.7 times smaller in 15 mm compared to 30 mm diameter drift tubes. Fluctuations of the space charge and, therefore, of the electric field lead to variations of the drift velocity causing a deterioration of the spatial resolution in non-linear drift gases like Ar:CO_2 (93:7) where the drift velocity depends on the electric field. This effect increases strongly with the drift distance above a value of 7.5 mm while the gain drop effect on the spatial resolution dominates for distances close to the sense wire (see Fig. 26, left) [19, 12, 13]). For 15 mm diameter tubes with drift radii below 7.1 mm, the effect of space charge fluctuations is essentially eliminated leading to a reduction in the degradation rate of the average spatial resolution by another factor of 2.

Parameter	Design value
Tube material	Aluminum
Outer tube diameter	15.000 mm
Tube wall thickness	0.4 mm
Glue gap between tubes	0.1 mm
Wire material	Gold-plated W/Re (97/3)
Wire diameter	50 μm
Wire tension	300 ± 15 g
Gas mixture	Ar/CO_2/H_2O (93/7/$\leq$ 1000 ppm)
Gas pressure	3 bar (absolute)
Gas gain	2 x 10^4
Wire potential	2730 V
Maximum drift time	$\sim$ 185 ns

Table 9: The operating parameters of small-diameter MDT chambers.

For drift radii below 7.5 mm, i.e. for the 15 mm diameter tubes, the space-to-drift time relationship is close to linear leading to a reduced sensitivity to environmental parameters such as gas composition and density, magnetic field and irradiation rate variation (Fig. 25, right).

Since the spatial resolution of the drift tubes improves with increasing drift radius, the average single-tube resolution at low background rates is degraded from 83 μm for 30 mm diameter tubes to 110 μm for 15 mm diameter tubes after applying time-slewing corrections. Fig. 27 shows the dependence of the average 30 mm and 15 mm diameter drift tube resolution on the background hit rate measured at the GIF. The measurements for 15 mm diameter tubes agree well with the expectation from the 30 mm diameter tube measurements derived by averaging over the drift radius range $r < 7.5$ mm in Fig. 26 and scaling the corresponding background rates with the factor 8.7 to account for the reduced gain loss. The measurements confirm the expectation that the degradation rate of the spatial resolution with the background flux is reduced by a factor of 10 for 15 mm compared to 30 mm diameter tubes.

The average 15 mm diameter drift tube resolution is 143$\pm$4 μm at the maximum background hit rate of 10 kHz/cm^2 at which GIF measurements could be performed. At 14 kHz/cm^2 rate it
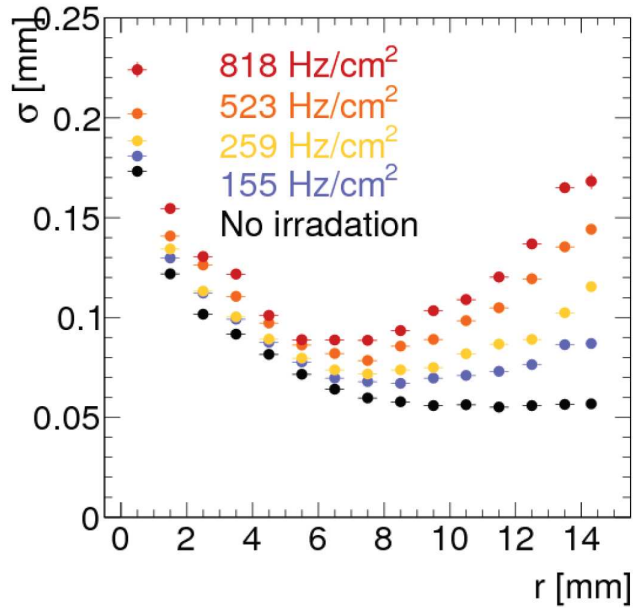
Figure 26: Spatial resolution of 30 mm diameter drift tubes (with time-slewing corrections) as a function of the drift radius for different background hit rates as measured at the GIF [12, 13].
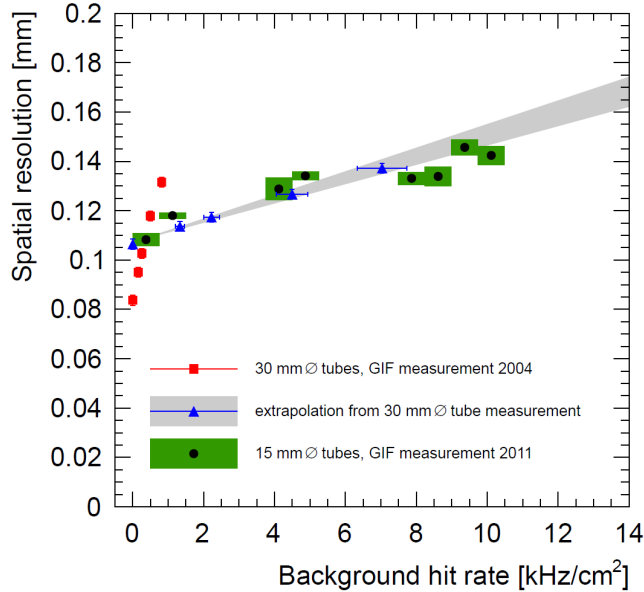

Figure 27: Dependence of the *average* drift tube resolution (with time-slewing corrections) on the background hit rate. The measurements for 30 mm and 15 mm diameter drift tubes at the GIF are compared.

will still be better than 170 μm. Consequently, the track point resolution of the sMDT chambers in the proposed NSW layout with 2 x 4 (2 x 6) tube layers for $R > 200$ cm ($R < 200$ cm) is better than 46 μm for $R > 160$ cm and better than 60 μm for smaller radii R in the NSW at the highest background rates corresponding to 14 kHz/cm^2 at the inner bore (see Fig. 28). The sMDT chamber resolution quoted corresponds to the average number of hits in the chambers as a function of the background counting rate taking into account the measured 3σ efficiency of the drift tubes (see Fig. 40). Fig. 28 also shows the sMDT chamber resolution for an optional

alternative layout with two additional tube layers per multilayer at $R < 160$ mm.

With the additional tube layers, the sMDT chamber resolution at $R < 160$ μm is improved to better than 50 μm. Without background irradiation, the sMDT chamber resolution is better than 40 μm over the whole NSW. The combination of the tracking information of the sMDT and trigger chambers will give considerable further improvement of the resolution.
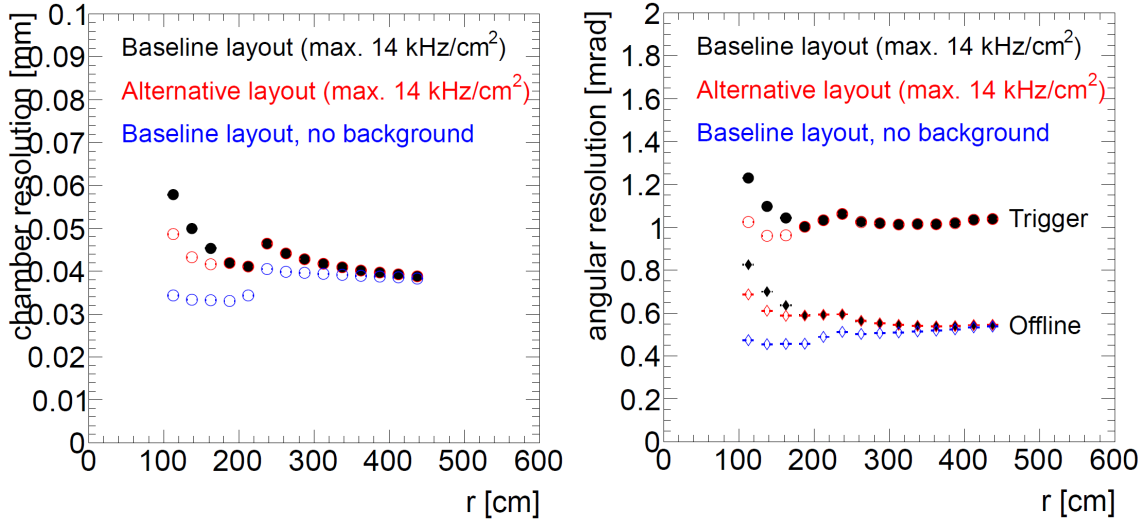

Figure 28: Radial dependence of the *average* point (left) and angular (right) resolution of the sMDT chambers in the NSW for the maximum background flux corresponding to 14 kHz/cm^2 at the inner bore and without background irradiation for the baseline layout and an alternative layout with two additional tube layers per multilayer at $R < 160$ cm. The spatial resolution is quoted for the average number of hits in the chambers depending on the background counting rate taking into account the measured drift tube efficiency. The angular resolution is shown for the maximum time resolution of the TDC used in the offline reconstruction and for 12.5 ns coarser time digitization for the use of the MDT chambers in the L1 muon trigger resolutions of the trigger chamber-sMDT system are also shown as a function of R.

The angular resolution is only relevant for the use of the MDT chambers in the future L1 muon trigger in combination with the trigger chambers. It is limited by the lever arm available for the drift tube chambers in the Small Wheels. On the trigger level, 1 mrad angular resolution is achieved in the radial range $R > 125$ mm corresponding to $\|\eta\| < 2.4$ covered by the L1 muon trigger.

B.2   Chamber Design

The design of the muon drift-tube chambers with 15 mm diameter tubes for the new Small Wheels follows as closely as possible the current ATLAS MDT chamber design in the endcap region of the muon spectrometer (Fig. 10). The chambers consist of two multilayers of four or six layers of drift tubes each in densest package. The aluminum tubes of 15 mm outer diameter and 0.4 mm wall thickness are produced according to industry standard and are chromatized for cleaning and reliable electric contact. The tubes are separated by 0.1 mm wide glue gaps

during chamber assembly. The two multilayers are separated by a spacer frame carrying the supports of the integrated drift-tube and trigger chambers on the Small Wheel structure and the in-plane optical alignment system monitoring the planarity of the chambers. The aluminum spacer frame is of similar design as for the present Small Wheel MDT chambers. Modification in the chamber design are mainly due to the four times denser packaging of the drift tubes and their gas and electrical connections.

Central to the chamber design is the design of the drift tubes and of their endplugs (see Fig. 11). The aluminum tubes of 15 mm outer diameter and 0.4 mm wall thickness are produced according to industry standards (DIN) with tolerances of ± 0.1 mm on diameter, roundness and concentricity of inner and outer circumference and of ± 0.5 mm on straightness and chromatized for cleaning and reliable electric contact. The endplugs insulate the sense wire from the tube wall, center the wire in the tubes, position it with respect to the external reference surface on the endplug with an accuracy of better than 10 μm and provide high-voltage-safe connections to the gas distribution manifold (see Fig. 29) and to the 24-channel readout and high-voltage interface boards ("hedgehog cards", Figs. 38).
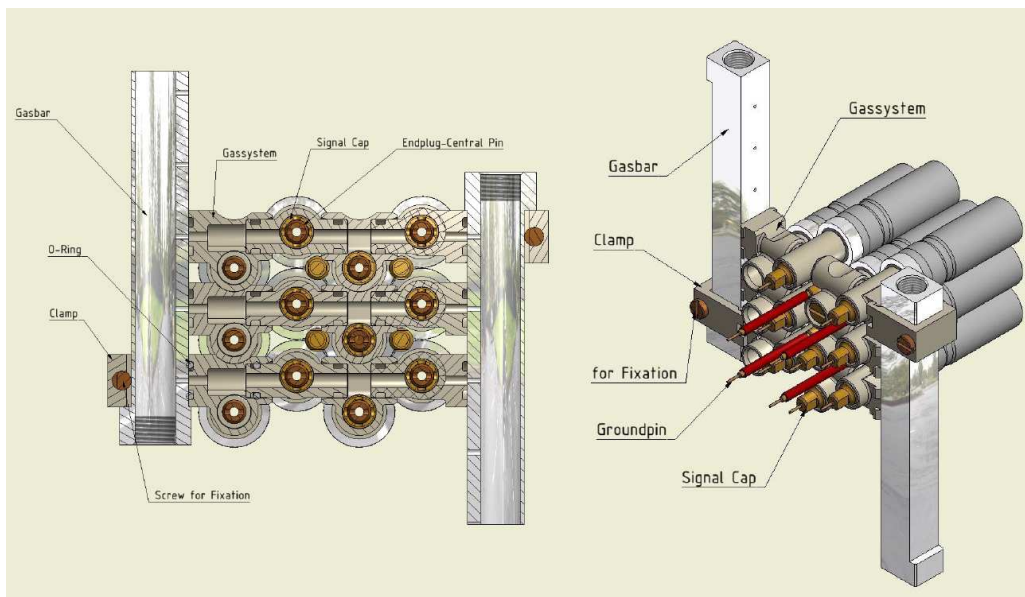

Figure 29: Design of the gas manifolds. The gas inlet and outlet bars are located at opposite ends of the tube multilayers.

The wire is fixed at both tube ends in copper crimping tubes inserted into the central brass inserts of the endplugs and connected to the signal and high-voltage hedgehog cards via brass signal caps which are screwed onto the brass inserts, sealing the tubes with respect to the gas manifold with O-rings. The brass insert of the endplug holds the spiral-shaped wire locator ("twister") in a central bore on the inside of the tube and transfers the wire position to the precisely machined reference surface at the outside of the tube which is used to accurately position the drift tubes during chamber assembly. The wire position information is transferred solely via the precision machined brass insert; precision machining of the complete endplugs is not necessary anymore, facilitating the production of the tubes and improving the accuracy of chamber construction. The two most critical problems for the ATLAS MDT drift tube production, cracking of the Noryl® plastic insulator and precision machining of the injection moulded endplugs, have been eliminated by the new design.

38

The insulators of the endplugs consist of Crastin®, a PBT based thermoplastic with 30 % glass fiber admixture to improve mechanical stability which shows little shrinkage and outgassing and, unlike Noryl® (material in the present MDT endplugs), high stability against cracking under stress. The material is of similar chemical composition as Pocan® which is used for the injection moulded components of the gas manifolds of the present and the new drift tube chambers. The endplugs are fabricated by injection moulding and sealed in the aluminum tubes with O-rings by circular mechanical crimping of the tube walls.

The modular gas distribution system consists of injection moulded plastic tubes made of Pocan® without glass fiber which interconnect adjacent tubes in the direction perpedicular to the multilayer and connect them to an aluminum gas distribution bar on the readout and the high-voltage end of the multilayer (see Figs. 29 and 30).

Figure 30: Picture of the gas manifold mounted on the prototype chamber.

The readout and high-voltage supply scheme follows closely the one of the present MDT chambers using the same parameters and specifications. The high-voltage decoupling capacitors on the readout side and the terminating resistors on the high-voltage supply end are individually encapsulated in plastic containers for high-voltage protection. The plastic containers are integrated with the hedgehog cards plugged onto the gold-plated pins of the signal caps and ground connectors. The ground pins are screwed into the gaps formed by three adjacent tubes (see Figs. 11 and 30) during chamber assembly to connect the tube walls to the ground of the hedgehog cards. This scheme allows for the high-voltage-free design of the readout hedgehog cards.

Each passive readout hedgehog card is connected to an active front end electronics board (mezzanine card) for 24 channels carrying new radiation hard ASICs, three 8-channel amplifier-shaper-discrimiator (ASD) chips and one 32-channel HPTDC chip (see below). The mezzanine cards follow one-to one the shape of the hedgehog cards and are already under development. The electronics boards are enclosed in chromatized aluminum Faraday cages which also shield the readout hedgehog cards from the mezzanine cards.

B.3 Readout Electronics

The readout of the Small MDT tubes will follow the proven architecture of the present MDT system. A number of additions and modifications, however, will be necessary in order to adapt the rate capability of the readout chain to the requirements of the SLHC. For the mechanical integration of the readout electronics with the Small tube chambers, the layout of the electronics will have to be adapted to the 4 times higher tube density at the ends of the Small tube chambers. Finally, the radiation tolerance of all components will have to comply with the high radiation levels, in particular at the inner border of the Small Wheel.

B.3.1 Architecture of the present MDT readout

In the present readout scheme tube signals are routed via a PCB ("hedgehog card") to a piggy-back card ("mezzanine card"), containing an Amplifier and Shaper, followed by a Discriminator with adjustable threshold, all three functions being integrated in a radiation tolerant ASIC (ASD). The discriminator outputs, in turn, are routed to a TDC, where each leading and trailing edge signal receives a high-precision time stamp, which is retained, together with the corresponding channel number, in a large internal buffer of the TDC ("Level-1 buffer").

When the TDC receives a Level-1 trigger, a subset of the recorded hits, corresponding to a pre-defined time window, are retained for readout and are forwarded to the data concentrator of this chamber, the "Chamber Service Module" (CSM). From there, data are sent to the off-chamber electronics in USA15, the "Readout Driver" (ROD). A CSM can serve up to 18 mezzanine cards. The operation parameters of the analog frontend (ASD) and the TDC are controlled by a JTAG string, which is distributed by the Detector Control System (DCS) to the CSM, which sends it individually to each mezzanine card. Fig. 22 gives the layout of the present system. A detailed presentation of the MDT readout electronics is given in [5]. The ASD and TDC ASICs are described in [7] and [8].

B.3.2 Architecture of the readout for sMDT chambers

For the evolution of this architecture into matching the requirements of the Small tube readout, a number of problems limiting the performance of the present scheme has to be overcome. Given the high rate capability of the Small MDT tubes, the bandwidth of the readout system has to be increased. Due to the limitations of the internal buffering scheme and processing speed, the present TDC can only handle average tube rates up to about 300 kHz per tube without losing data, while Small tubes would operate beyond 1 MHz per tube. Therefore, an improved TDC is an essential requirement for a new readout design. Another limitation of the readout bandwidth comes from the optical link, connecting the CSM to the ROD, as the S-link protocol only supports a usable bandwidth of 1,4 Gbit/s. Fig. 23 shows occupancy and efficiency of Large and Small tubes as a function of tube hit rate.

When upgrading the performance of ASICs (ASD, TDC), we have to take into account that their technologies are no longer supported by industry. The following new components had therefore to be introduced into the readout system.

(a) The ASD is re-designed in the IBM 130 nm technology. A 4-channel prototype, demonstrating the analog parameters, has already been produced and tested and works correctly. Most analog parameters of the previous design are preserved. The 4-channel version of the complete ASD chip has been delivered and bonded and is ready for testing.

(b) The TDC will be replaced by the HPTDC, designed by the CERN-MIC group ([6]). This 32-channel device has an improved internal buffering scheme as well as higher transfer and processing speeds.

(c) The CSM collects data from a MDT chamber formats the event and sends data, trigger-by-trigger, via an optical link to the ROD in USA15. All logical operations are performed by an FPGA, which will need to be upgraded to higher radiation tolerance. The interface to DCS, needed for controlling electrical and temperature parameters on the chamber will be done via the GBT (see below). The adapter box to the CANbus (ELMB) can therefore be dropped, reducing complexity of cabling.

(d) The link connecting the CSM to the ROD will be replaced by a GigaBit Transmitter link (GBT), developed by CERN. This link provides a 3 times higher transfer rate (Gbit/s), compared to the S-link [9].

Another stringent requirement for the realization of the new readout scheme is the mechanical integration of the on-chamber readout electronics with the chamber mechanics, as the density of channels at the tube ends is four times higher than in the case of the Large tubes. The following design changes will therefore be implemented.

(a) HV decoupling capacitors are located in 15 mm diame'ter cylinders at the tube ends, see Fig. 38. The density of signal routing on hedgehog cards is thus no longer limited by HV insulation distances between HV and signal traces on the PCB.

(b) To match the higher tube density, the space on the mezzanine card has to be used more efficiently. For this purpose, the passive protection circuitry of the ASD inputs will be moved to the hedgehog card. In addition, the modularity of the ADSs will be changed from 8 to 16 channels per chip, which goes well with the 32-channel modularity of the HPTDC.

(c) For the interconnection between mezzanine cards and New CSM we foresee to use the same 40-wire cables as was used in the present system. Its moderate diameter and high flexibility may be important for fitting the new MDTs into the limited space in the Small Wheel.

B.4   Chamber Construction

B.4.1   Drift tube production

The drift tubes are fabricated and tested in a climatized clean room of class 10000 using a semi-automated assembly station (Fig. 31). The wires are fed through the tube by air flow without touching them by hand. Wire tensioning and crimping is performed fully automatically. After fabrication, the tubes are immediately tested for wire tension, gas tightness and leakage currents under high voltage (see below). A production speed of 120 drift tubes per day has already been achieved.
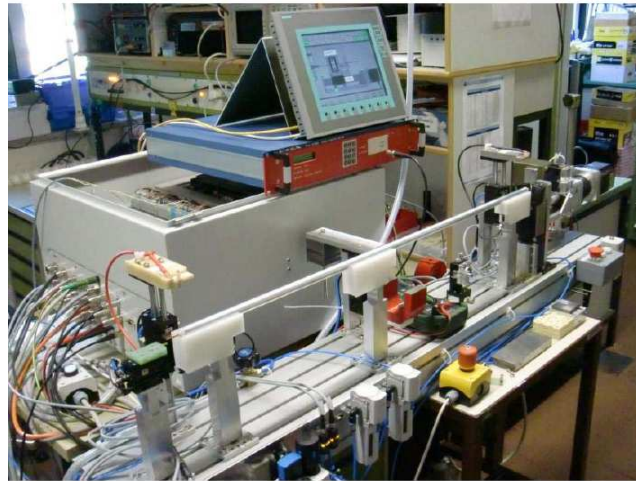

Figure 31: Semi-automated drift tube assembly station.

B.4.2   Chamber assembly

The individual tubes are assembled to chambers using precision jigs on a flat granite table in a climatized clean room as shown in Figs. 32. The jigs are machined with an accuracy of better than 10 μm. The two multilayers are assembled and glued together within one working day using two identical jigs. The assembly procedure is illustrated in Fig. B.4.3. The jig elements which position the endplugs and sense wires of each layer in the transverse plane are stacked layer-by-layer forming a precise two-dimensional grid. Bearings for mounting of the trigger chambers and, for the first multilayer, platforms holding the external alignment sensors are glued to the bottom tube layers positioning them precisely with respect to the assembly jigs and, consequently, to the wires.

On the second day, after letting the glue cure over night, the spacer frame is glued to the top of the first multilayer in its jig and the in-plane alignment system is calibrated. The second multilayer is removed from the jig and glued to the top of the spacer, aligning it precisely with respect to the assembly jig and thus to the first multilayer. Monitoring of the tube and layer positions like during the ATLAS MDT chamber production is not necessary with this assembly scheme as has been demonstrated by the protyotype chamber construction (see below). However, it is foreseen to measure during assembly the heights and angles of the stacked

jigs with feeler gauges with respect to the granite table. Also the alignment platform positions and their angular orientations will be measured with feeler gauges with respect to the granite table and thus to the wires like it has been done for the BOS and BOF MDT chambers.
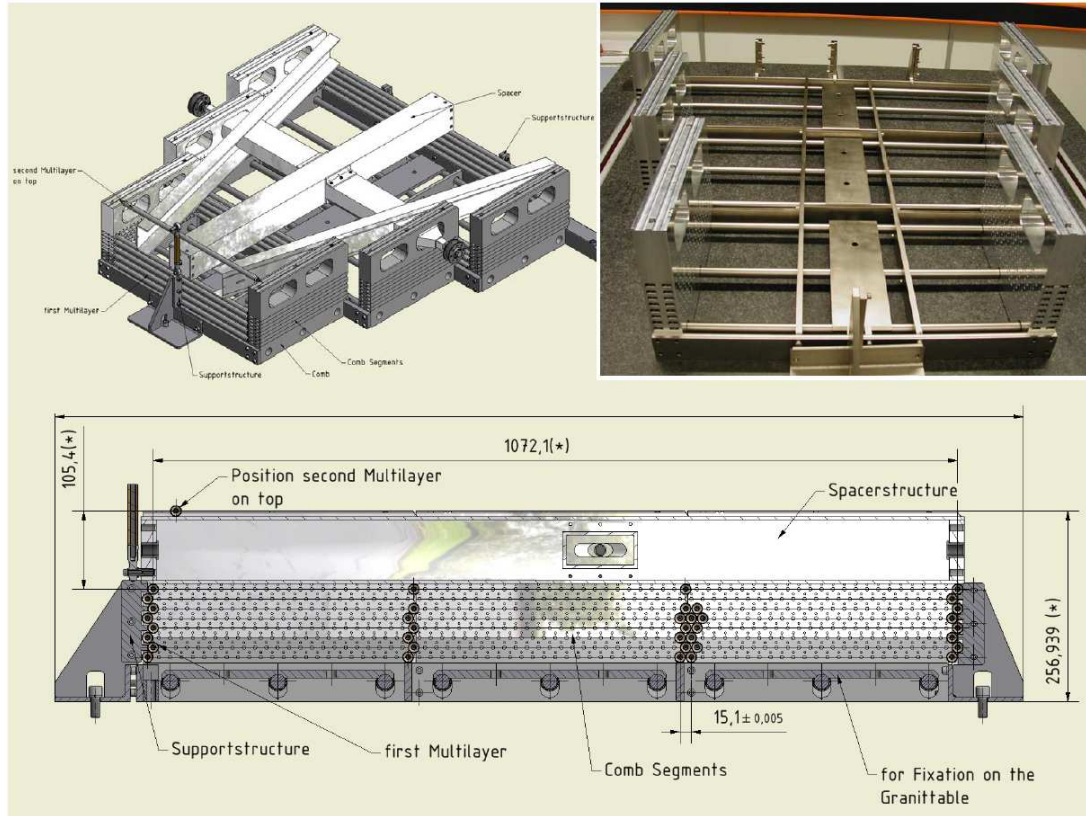

Figure 32: Assembly tooling for the sMDT chambers with precise positioning of the endplugs of the drift tubes holding the sense wires. The jigs are modular and adjustable for the construction of different chamber types. References for the precise mounting of the alignment sensor platforms with respect to the wires are part of the jig design.

After the assembly of the drift tubes, the mounting of the gas manifolds and testing for leak tightness requires about one week. Another two weeks are foreseen for mounting of the hedgehog cards, installation of the Faraday cages and cabling of the chamber. Mounting of the trigger chambers on the drift tube chambers and combined test will likely be performed at CERN.

B.4.3   Prototype chamber construction

A full-scale prototype of a 15 mm diameter drift tube chamber for the innermost region of the Small Wheels presently covered by CSC chambers has been constructed in 2010 (see Figs. B.4.3 and tested in the CERN Gamma Irradiation Facility GIF as well as in the H8 testbeam in 2010 and 2011. The chamber consists of 2 x 8 layers of drift tubes and is readout with the existing MDT mezzanine cards and Chamber Service Module (CSM). With this prototype chamber all aspects of the chamber design and performance as well as the construction and test procedures have been verified and the required time and manpower for chamber production and test has

been evaluated in detail. With a semiautomated drift tube assembly station, more than 100 drift tubes have been routinely produced per day. The tubes assembled every day will be tested for gas tightness and leakage currents under high voltage in an automated test stand over night.

The wire positions in the two larger trapezoidal sectors of the prototype chamber equipped with readout electronics have been measured using 600k cosmic ray muon tracks in the cosmic ray test stand at LMU Munich. In the horizontal (y) direction, the individual coordinates have been determined with an accuracy of about 5 microns (see Fig. 34). In the vertical (z) direction, the layer-to-layer distances have been measured with similar accuracy (see Fig. 35). Two BOS MDT chambers with known wire positions from X-ray tomograph measurements were used as tracking references. The same setup has been used to measure the wire positions in all ATLAS BOS and BOF MDT chambers. It will also be used to measure the positions of the wires and of the alignment sensors of the chambers for the NSW.
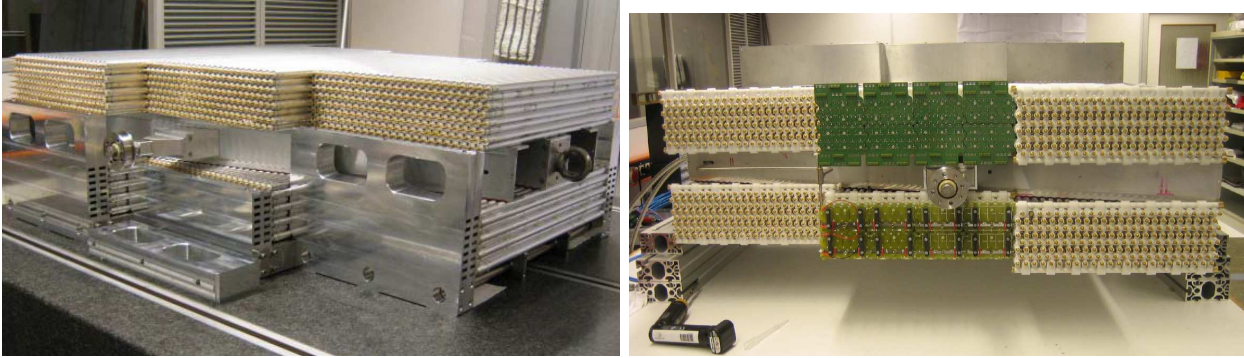

Figure 33: The sMDT prototype chamber during and after assembly, consisting of two multilayers with 8 tube layers each, 72 tubes per layer and 1152 tubes in total.

The geometrical parameters of the chamber given in Table 10 have been determined from a fit to the measured wire positions. They are in excellent agreement with the design values in y direction. In z direction, where the measurement accuracy is less, there are minor deviations. The distributions of the residuals of the measured wire positions in y direction and of the measured layer-to-layer distances in z direction with respect to the ideal grid (left) and to the measured grid (right) are shown in Figs. 36 and 37, respectively. All tracks crossing the chamber over the whole tube length were used for the wire position measurement which therefore comprises wire positioning uncertainties at both tube ends. The uncertainty in the wire sag is below 5 μm. The wire positioning accuracy at each chamber end is thus given by the width of the residual distribution devided by $\sqrt{2}$. It is better than 20 μm in y and z direction. The residuals are nicely Gaussian distributed around zero and show no significant systematic deviations from the expected grid.

B.4.4   Interfacing with the readout electronics

The readout and high-voltage supply scheme follows closely the one of the present MDT chambers using the same parameters and specifications. The high-voltage decoupling capacitors on the readout side and the terminating resistors on the high-voltage supply end are individually encapsulated in plastic containers for high-voltage protection. The plastic containers are integrated with the hedgehog cards plugged onto the gold-plated pins of the signal caps and ground

Parameter	Nominal value [mm]	Measured value [mm]
Wire pitch y	15.100	15.1018 ± 0.0003
Wire pitch z	13.077	13.091 ± 0.007
Relative layer shift y	7.550	$7,550 \pm 0.0005$
Multilayer z distance	90.400	90.382 ± 0.010
σ_y w.r.t. nominal grid	0.020	0.018
σ_y w.r.t. fitted grid	0.020	0.016
σ_z w.r.t. nominal grid	0.020	0.016
σ_z w.r.t. fitted grid	0.020	0.013

Table 10: Geometrical parameters of the sMDT prototype chamber. The values measured using cosmic ray muon tracks agree very well with the design values. The uncertainties in the wire coordinates in y and in the layer distances in z direction at each chamber end with respect to the nominal and to the measured grid, respectively, are also given.
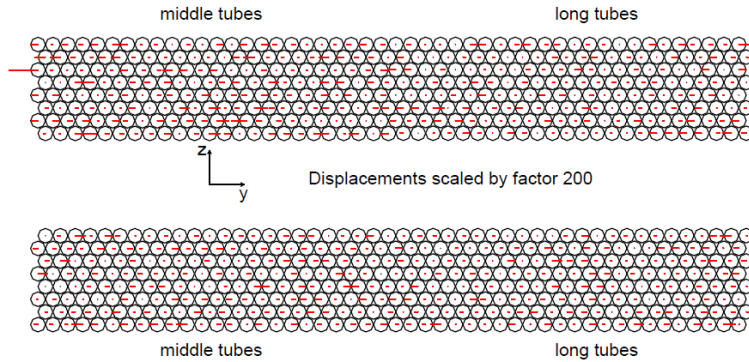

Figure 34: Residuals of the measured wire coordinates in the horizontal (y) direction with respect to the fitted wire grid using 600k muon tracks registered in the cosmic ray test stand.
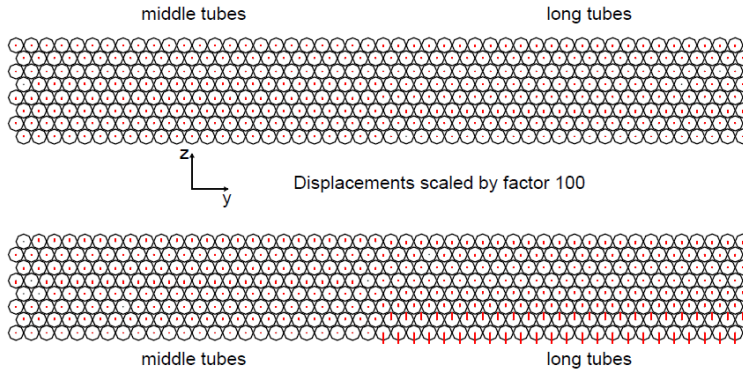

Figure 35: Residuals of the measured wire coordinates in the vertical (z) direction with respect to the fitted wire grid using 600k muon tracks registered in the cosmic ray test stand.

connectors. The ground pins are screwed into the gaps formed by three adjacent tubes during chamber assembly to connect the tube walls to the ground of the hedgehog cards (Fig. 38. This scheme allows for the high-voltage-free design of the readout hedgehog cards.

Each passive readout hedgehog card is connected to an active front end electronics board (mezzanine card) for 24 channels carrying new radiation hard ASICs, three 8-channel amplifier-
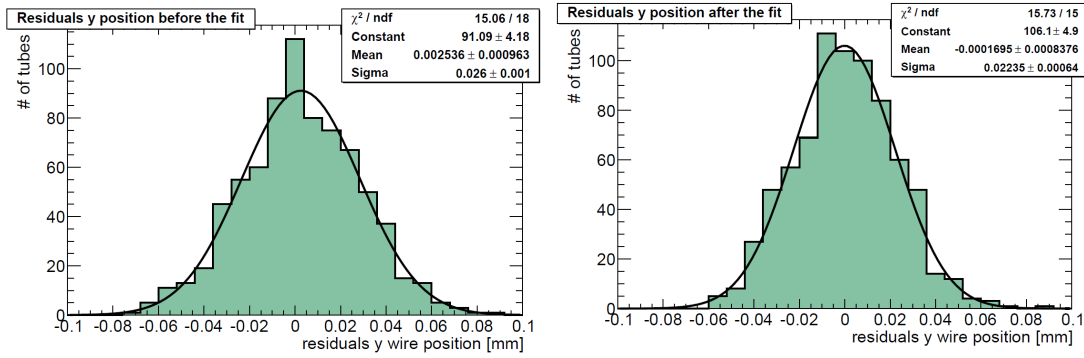
Figure 36: Residual distributions of the wire coordinates in y direction with respect to the nominal (left) and to the fitted (right) wire grid from the cosmic ray measurements. The widths of the distributions include the measurement errors.
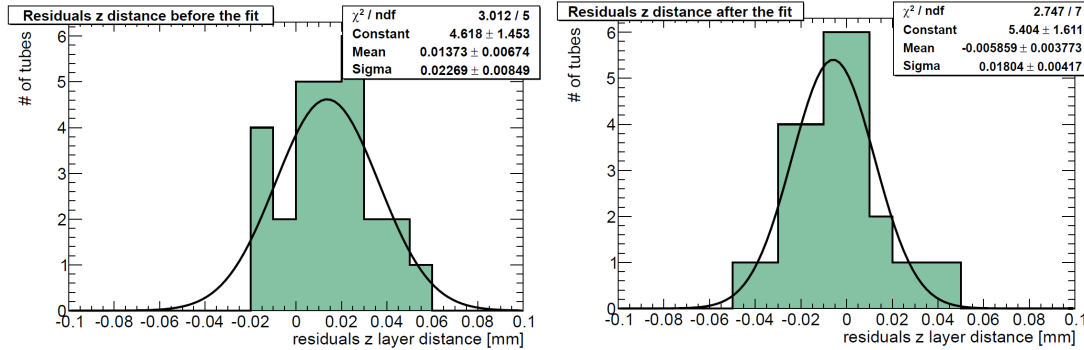

Figure 37: Residual distributions of the layer-to-layer distances in z direction with respect to the nominal (left) and to the fitted (right) wire grid from the cosmic ray measurements. The widths of the distributions include the measurement errors.

shaper-discrimiator (ASD) chips and one 32-channel HPTDC chip (see below). The mezzanine cards follow one-to one the shape of the hedgehog cards and are already under development. The electronics boards are enclosed in chromatized aluminum Faraday cages which also shield the readout hedgehog cards against the mezzanine cards.

B.4.5   Sharing of work and logistics between production sites

The construction of the 96 drift tube chambers with approximately 70000 drift tubes of lengths between 0.5 m and 2.2 m for the new Small Wheels can be performed at three main construction sites, the MPI Munich, the University of Freiburg and IHEP Protvino, in the years 2013 to 2016. The intergration of the sMDT and trigger chambers at CERN will proceed in parallel. With additional institutions joining the project, the chamber construction can proceed faster. 2-3 FTE manpower per construction site are planned for the chamber construction.

LMU Munich and the University of Würzburg will contribute to the testing of drift tubes and completed chambers before and after shipment to CERN as well as to chamber integration and commissioning of the Small Wheels at CERN. The relative wire positions of all sMDT chambers and the positions of the alignment sensors relative to the wires will be measured with an accuracy of about 5 μm in the cosmic ray test stand at LMU Munich like for the ATLAS

46

BOS and BOF MDT chambers built in Munich and for the sMDT prototype chamber (see below). A cosmic ray test stand will also be set up at CERN for the test of the integrated chamber modules before installation. The measurement of the sMDT wire and alignment sensor positions also in this test stand, with two MDT chambers with known wire positions as reference like in the setup at LMU Munich, is under consideration. In both test stands also the relative positions of sMDT and trigger chambers and of the internal geometry of the trigger chambers can be measured with high accuracy.
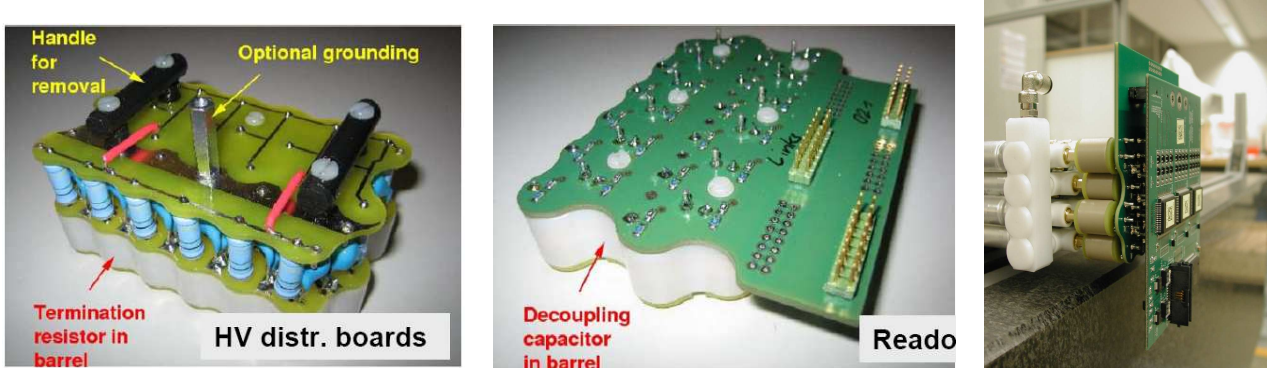

Figure 38: High voltage (left) and signal (middle) distribution boards, the "hedgehog cards", to be mounted at the two ends of the tubes (right). The plastic cylinders containing the decoupling capacitors and the terminating resistors, respectively, are integrated on the PCB boards.

The participating institutes have extensive experience with the construction of the ATLAS MDT chambers as well as the associated quality assurance procedures. The required clean rooms and test equipment and the design of tooling for chamber construction and testing already exist. The University of Freiburg and MPI Munich will also be involved in the design, fabrication and measurement of the alignment reference bars for the new Small Wheels in collaboration with Brandeis University.

B.5   Quality Assurance and Commissioning

The quality assurance and commissioning procedures follow closely the specifications for the ATLAS MDT chamber production [21]. Each tubes will be tested with respect to wire tension, gas tightness and leakage currents under high voltage before installation in a chamber. The full quality control procedures have already been developed and tested during the sMDT prototype chamber construction. Due to the new design of the endplugs and of the chamber assembly tooling, wire position measurement for individual drift tubes and monitoring of the tube positioning during assembly, as performed during the ATLAS MDT chamber production, are not necessary anymore as was demonstrated by the sMDT prototype chamber construction.

The hedgehog cards and the mezzanine readout boards with the new radiation hard ASD and HPTDC chips as well as the new chamber service modules CSM (see below) will be desiged, produced and tested by MPI Munich. New improved noise filters for the high-voltage supply lines for each chamber layer have been designed and will be produced at MPI Munich.

The completed chambers will be tested for broken wires, gas tightness, leakage currents and noise rate before and after delivery to CERN. In addition, all chambers will be tested in cosmic ray test stands at LMU Munich and CERN. The individual wire positions of the sMDT chambers and the positions of the alignment sensors relative to the wires will be measured with an accuracy of about 5 μm using two MDT chambers with known wire positions as reference as it was done sucessfully for all ATLAS BOS and BOF MDT chambers built in Munich and for the sMDT prototype chamber. The geometrical chamber parameters will be determined with submicron precision in this way.

Bundles of drift tubes will be mounted on the alignment platforms in the same way as the alignment sensors themselves allowing for the precise direct determination of the sensor positions relative to the sMDT wires in the cosmic ray test stands. A method using stereo X-ray sources and calibrated references wires as developed at Brandeis University is also under consideration for measuring the alignment sensor positions realtive to the sMDT wires. After integration, also measurement of the positions of the trigger chambers with respect to the wires in the drift tube chambers and of the internal geometry of the trigger chambers in the cosmic ray test stands is foreseen.

2-3 FTE manpower at each of the 4 core production sites are planned for chamber testing and commissioning.

B.6   Operation, Maintenance and Safety

Due to their robust design and the high quality assurance standards during construction and commissioning, the ATLAS MDT chambers operate with very high reliability and data taking efficiency. The same design, fabrication and testing procedures will be applied for the small diameter drift tube chambers. Also maintenance and repair procedures will be the same in principle as for the existing MDT chamber system with improvements in the access to the CSMs and the HV splitter boxes as well as to the chambers in the inner regions of the new Small Wheels.

The modular structure of the chambers provides a high degree of redundancy. Each multi-layer of a chamber will be supplied by a separate high voltage channel, the innermost chambers by two channels because of the higher currents. 384 HV channels are needed for both Small Wheels.

In the chamber layout and the design of the Small Wheel structure, accessibility of the Faraday cages of the drift tube chambers for exchange of electronics boards or for disconnecting individual drift tubes has been taken into account. The chamber service modules (CSM) together with the DCS boxes of all chambers will be installed in better accessible and more radiation-safe regions at the outer rim of the Small Wheel. There will be 2 CSMs per chamber, one per multilayer, such that only one multilayer is lost until a broken CSM is replaced during an ultrashort access.

The individual tube layers are independently connected to the high-voltage. The splitter boxes for the HV channels will be located at the outer rim of the new Small Wheels. If a wire breaks, which is a very rare event, only one tube layer will be lost after disconnecting it from

the HV splitter in an ultrashort access. During winter shutdown and opening of the Small Wheel, the affected tube can be disconnected from the high-voltage and the rest of the tube layer can be reconnected.

Gas leaks in the present MDT chambers are mainly due to cracks in injection moulded Noryl® endplugs and gas connectors. The drift tubes in the new Small Wheels are mechanically protected from the outside by the trigger chambers. To avoid gas leaks due to cracks in endplug insulators and gas connectors, thermoplastics with much better robustness against cracking than in te present MDT chambers have been chosen (see B.2, above). In addition due to their smaller volume, the 15 mm diameter endplugs are less prone to mechanical stress and cracks in the injection moulded plastic insulators than the 30 mm diameter endplugs.

Component	Comment (redundancy, accessibility)	Loss in coverage	Recovery procedure
CSM (with DCS box)	2 CSMs per chamber, 1 CSM per multilayer (ML)	1 multilayer	Repair in US access CSMs at outer rim
Mezz. card		24 chan.s in 1 ML	Repair in WS
LV supplies	2 CSMs (in diff. chambers) per channel	2 ML in diff. chambers	Repair in US access
HV supplies	$1 - 2$ channels per ML	$0.5 - 1$ ML	Repair in US access
Broken wire	HV distr. per layer using splitters at SW outer rim	$0.5 - 1$ ML before, $0.5 - 1$ layer after layer disconnect	Disconnect tube layer in US access Discon. tube from HV Repair in WS
Gas leaks	1 gas line per sect. and ML, 1 valve per ML at outer rim	1 ML of 1 sect. before, 1 ML of 1 chamb. after closing valve	Close valve of leaking ML in US access Repair in WS

Table 11: Risk analysis for the sMDT system in the new Small Wheels. The redundancy and accesibility of the critical components and the maximum loss in detector coverage in case of component failure are given as well as the recovery procedures (US = ultrashort, WS = winter shutdown).

The existing recirculating gas system with one volume exchange per day can be fully reused. Each multilayer of a Small Wheel sector will be supplied separately with gas using 16 gas lines for each new Small Wheel. Each multilayer of a chamber has a valve located at the outer rim of the Small Wheel. The total gas volume of the sMDT chambers in one new Small Wheel is 6750 l, 4000 l less than for the MDT chambers in one present Small Wheel.

The risk assessment for the sMDT chamber system for the new Small Wheels is summarized in Table 11 including the measures for minimizing the risk and reducing it even further than in the present Small Wheels.

B.7 Detector Performance

In order to verify the performance of the sMDT chambers, extensive tests of the full-scale prototype chamber with 15 mm diameter drift tubes have been performed in 2010 and 2011 in the H8 high-energy muon beam without background irradiation (see Fig. 39, left) and, using cosmic ray muon tracks, in the CERN Gamma Irradiation Facility (GIF) with a 500 GBq ^{137}Cs γ source (Fig. 39, right). Standard ATLAS MDT readout electronics has been used with the adjustable deadtime set to the minimum value corresponding to an overall effective deadtime of 200 ns. The spatial resolution and the efficiency of the individual drift tubes have been measured for increasing γ background counting rates up to 1200 kHz/tube at uniform illumination corresponding to 17 kHz/cm^2 in tubes of 0.5 m length like at the innermost radius of the new Small Wheels.

Fig. 40 shows the 3-σ efficiency of 15 mm diameter drift tubes and the track segment reconstruction efficiency as a function of the γ background counting rate in comparison with the results for the 30 mm diameter tubes from previous tests of a BOS MDT chamber at GIF with the X5 muon beam [12], [13]. The measurements were performed using as external tracking reference the other drift tube layers of the prototype chamber and a silicon strip detector beam telescope for the BOS chamber in the X5 beam, respectively. At low background rates, the 3σ tube efficiencies of 30 and 15 mm diameter tubes are 94 %. The efficiency loss is due to δ-rays created by interaction of the muons with the tube walls which produce hits earlier than the muons. The degradation of the efficiency with increasing rate shows the expected linear behaviour. The redundancy of track measurements in different tube layers allows for a better than 99 % track segment reconstruction efficiency up to the highest expected background rates at high-luminosity LHC.
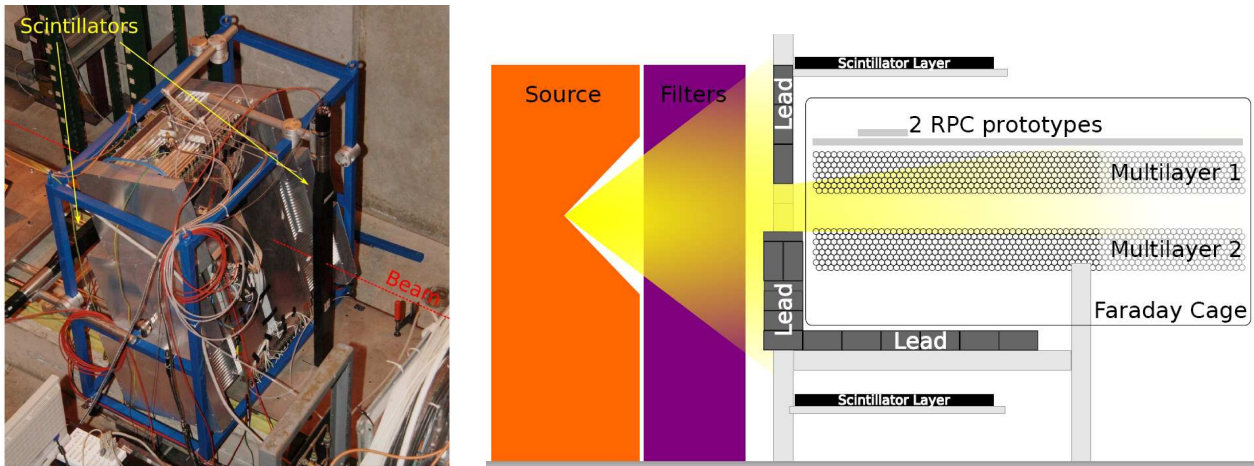

Figure 39: The test setups with the sMDT prototype chamber in the H8 muon beam at CERN (left) and in the GIF using a cosmic ray muon trigger (right).

As a measure for evaluating the tracking efficiency, we define the "3σ-efficiency" as the probability of detecting a tube hit within a distance of 3 times the drift tube resolution σ from the muon track, the muon track being defined by the other tubes on the track, extrapolated to the active volume of the tube. Similarly, the drift tube resolution as a function of the drift radius is determined by an iterative method excluding the evaluated tube from the track reconstruction in the chamber [22].
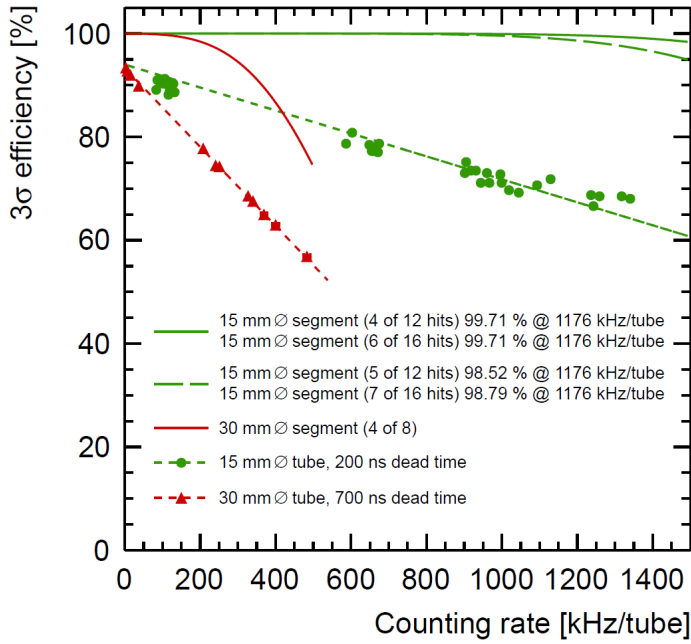
Figure 40: The 3σ efficiency of individual drift tubes as measured at the GIF as a function of the background counting rate. Results for 15 mm and 30 mm diameter tubes are compared. The corresponding calculated track segment reconstruction efficiencies in 2 x 4 layer MDT chambers and in sMDT chambers with 2 x 6 or, optionally, 2 x 8 tube layers are also shown.

Figure 41: Spatial resolution (with time-slewing corrections) as a function of the drift radius of large and small diameter drift tubes measured without background irradiation in the X5 and in the H8 muon test beam, respectively, in comparison with simulation results using GARFIELD. Time-slewing corrections improve the average drift tube resolution by 20 μ both for the larger and the smaller diameter tubes.

In Fig. 41 the spatial resolutions of 15 mm and 30 mm diameter drift tubes measured as a function of the drift radius r and without background irradiation in the CERN high-energy muon beams H8 and X5, respectively, are compared. The track impact radius was determined using as external references the other drift tube layers of the prototype chamber in

51

the H8 beam and, respectively, a silicon strip detector beam telescope in the X5 beam. The radial dependence of the 15 mm diameter tube resolution agrees with the 30 mm diameter tube resolution measurement for $r < 7.5$ mm and with the GARFIELD simulation [16]. The comparison of the resolution curves is performed without time-slewing corrections applied. Corrections for time-slewing using the pulse-height information provided by the MDT readout electronics improve the average drift tube resolution by 20 μ both for the larger and the smaller diameter tubes. The average spatial resolution of the of 15 and 30 mm diameter tubes at low background rates is 110 ± 2 μm and 83 ± 2 μm, respectively, taking into account the time-slewing corrections (see Fig. 40).

The dependence of the spatial resolution of the 15 mm diameter drift tubes has been measured at the GIF using the unirradiated regions of the prototype chamber as tracking reference for cosmic muons. The measurements extended up to a background flux of 10 kHz/cm^2 at which an average drift tube resolution of 143 ± 4 μm has been obtained. At 14 kHz/cm^2 rate it will still be better than 170 μm (see Fig. 27).

Component	Nr. of units	Cost/unit (CHF)	Total cost (kCHF)
Al tubes	71000	3.6	256
Wire	5.5 km	488/km	3
Endplugs	141312	7.2	791
Gas connectors	141312	1.8	113
Spacer, supports	96	1000	96
Faraday cages	2 x 96	500	96
Tooling	2	25000	50
Detector mechanics			1405
HV&RO hedgehog boards	5888	100	589
Mezzanine cards w. cable	2944	240	706
CSMs	160+32	1100	211
MRODs/CSM	160	1200	192
Electronics& readout			1698
Gas distribution system/ML	2 x 96	300	58
LV&HV power supplies w. cables/CSM	160	2000	320
DCS modules w. fiber link/CSM	160	400	64
Services			442
In-plane sensors/chamber	96	909	87
External alignment sensors	4 x 96	455	175
Multiplexers/chamber	96	455	44
Alignment (on-chamber)			306
Total			3851

Table 12: CORE cost of the sMDT chamber system including services, readout and alignment components.

B.8 Ageing Tests

Ageing is not expected to occur in aluminum drift tubes with clean $Ar:CO_2$ gas. No ageing has been observed in test of the MDT tubes up to a collected charge on the wire of 0.6 C/cm. Only endplug and gas system materials with little outgassing which have already been certified for the ATLAS MDT chambers are used and strict cleaning procedures are applied for all components in order to prevent contamination of the drift gas. There esists extensive experience on material selection and cleaning procedures from the ATLAS MDT chamber construction and commissioning.

Ageing tests of the new drift tubes with a 25 MBq and a 200 MBq ^{9}0Sr source are in progress. Until 27 January 2012, 1.38 C/cm of charge has been accumulated on the wires without sign of ageing. With the 200 MBq source, currently 0.025 C/cm are accumulated per day at a current of 3.1 μA per tube.

B.9 Cost, Funding, and Manpower

The costs of chamber mechanical components, on-chamber electronics, power supplies and DAQ system are summarized in Table 12. The cost estimates are based on tenders as well as on the actual cost figures of the ATLAS MDT chamber components.

Institute	FTE	Contribution
MPI Munich	5	Mechanics, electronics, L1 trigger design
	7	Chamber construction, test, integration, installation, alignment system, electronics production, HV/LV system
LMU Munich	3-4	Chamber construction, test, integration, installation
Freiburg U.	5-6	Chamber construction, test, integration, installation, gas system, DCS, alignment system
Würzburg U.	3	Chamber, electronics test, integration, installation, HV/LV system
IHEP Protvino		Chamber construction, test, installation
NIKHEF		MRODs design, production, test, installation
Tokyo		L1 trigger and electronics design and implementation
Brandeis U.		Alignment system

Table 13: Manpower for sMDT design, production, integration and installation.

Manpower cost for chamber assembly and test and for the testing of the electronics boards is not included The manpower allocation foreseen for this work at the participating institutes is shown in Table 13. The infrastructure of climatized clean rooms and the cosmic ray chamber test facility already exist as well es experienced technical personell. The design of the chambers and of the assembly tooling is performed at MPI Munich. The signal and high-voltage distribution (hedgehog) boards, the readout (mezzanine) cards, the amplifier-shaper-discriminator (ASD) chip and the chamber service module (CSM) are already under development at MPI.

A close collaboration exists between the MDT institutes and the TGC as well as the RPC

Item	2012	2013	2014	2015	2016	2017	2018	Total
Detector mechanics	100	400	500	405				1405
Electronics& readout		200	400	500	406	192		1698
Services				64	150	228		442
Alignment (on-chamber)		70	80	80	76			306
Total	100	670	980	1049	632	420		3851

Table 14: CORE cost time profile for the sMDT chambers (kCHF).

institutes on integrated chamber design and layout and on a common test program at the GIF and the H8 test beam.

Time of completion	Task
2010	sMDT Chamber design, prototype construction and test
2011	Integration sMDT amd trigger chambers,
	full ASD FE chip (4 channels)
2012	Construction of sMDT chambers for elevator regions,
	NSW design and chamber layout,
	full 8-channel ASD chip
2014	CSM design incl. MDT based L1 trigger functionality
2013–16	Chamber construction and integration, electronics production
2017–18	Integration and installation of NSWs at CERN

Table 15: Time schedule for sMDT chamber development amd construction.

A large fraction of the funding of the sMDT system is expected from the German funding agency BMBF and from MPI Munich in the period 2012–2016. The funding request to the BMBF for the period 2012–2015 has been submitted in December 2011. NIKHEF has expressed interest to contribute the MRODs for the sMDT chamber readout. Brandeis University and the University of Freiburg plan to contribute the optical alignment system including the alignment reference bars. The expected CORE cost spending profile is given in Table 14, the time schedule for development and construction in Table 15.

C The sTGCs for the New Small Wheel

In this section of the Appendix we present more technical details about the sTGC concept.

C.1 Latency of the sTGC trigger and the sTGC trigger demonstrator

To be used in phase I of the LHC upgrade, the overall trigger latency must be less than $2.55\,\mu s$. This means for the sTGC trigger that the signals from the chamber frontend must arrive at the input of the Sector Logic in USA15 not later than $1.05\,\mu s$ after the occurrence of the collision at the interaction point. Table 16 lists the delays contributing to the sTGC latency.

	Min	Max	Notes
TOF from interaction point to SW (10 m)	35	35	
propagation delay in chamber	25	25	
ASD	10	10	
on-chamber cabling (1.5-2.5 m) to selector	8	13	5 nsec/m
up- to down-stream package (50 cm)	0	3	
delay for pad trigger and deskew	15	25	
"deserializer" e.g. 1:10	11	12	10×1 ns "deserialized" to 10-bit
latency for the last sample of the pulse	64	100	depends on shaping time
accumulate the last 10 ns sample into ToT	10	10	
selector	5	10	switch
serializer to off-chamber logic	5	10	
on-chamber to off-chamber link	0	0	along the 90 m fibre below
deserializer	5	10	
find valid centroids and centroid averages	32.5	65	8 layers in parallel, 13 clocks
difference of centroid averages	2.5	5	
calc sub-ROI pointed to Big Wheel (LUT)	5	5	data sheet BRAM access 2 nsec
output serializer	50	75	GBT: 3 40 MHz clocks
fiber to Sector logic 90 m	495	495	5.5 nsec/m
	778	**908**	

Table 16: sTGC Latency - The table shows the delays (in ns) contributing to the latency of the precision strip trigger logic from the interaction point to the Sector Logic in USA15. All numbers are estimates except that for the centroid finder which has been measured for the demonstrator.

A demonstrator for sTGC trigger concept has been built and the latency of a realistic centroid finding and averaging algorithm has been measured. A block diagram of the demonstrator is shown in Fig. 42 and a photograph in 43. The centroid is the sum of each strip's "charge" weighted by the strip position. The division by the total charge is done using a Look-up-Table. The algorithm calculates with more than reasonable precision (12 bits for expressing the fraction of a strip part of the coordinate) and includes offsets for each layer and two overlapping channels on each edge. Isolated clusters of up to five strips are considered valid. Only the 1, 2, 3, or 4 valid centroids are selected for inclusion in the average of the centroids. The measured

latency of the algorithm whose input is the time-over-threshold values and output is the average of the valid centroids, is 13 clocks. The current clock is 5 ns (200 MHz) but the optimization of the number of clocks versus clock rate has not been completed. The demonstrator was connected to an sTGC quadruplet and was triggered by cosmic rays. Fig. 44 shows the four input strip profiles and the four calculated output centroids for a cosmic ray.

The next generation demonstrator for developing trigger algorithms and processing will be a completely custom board design.
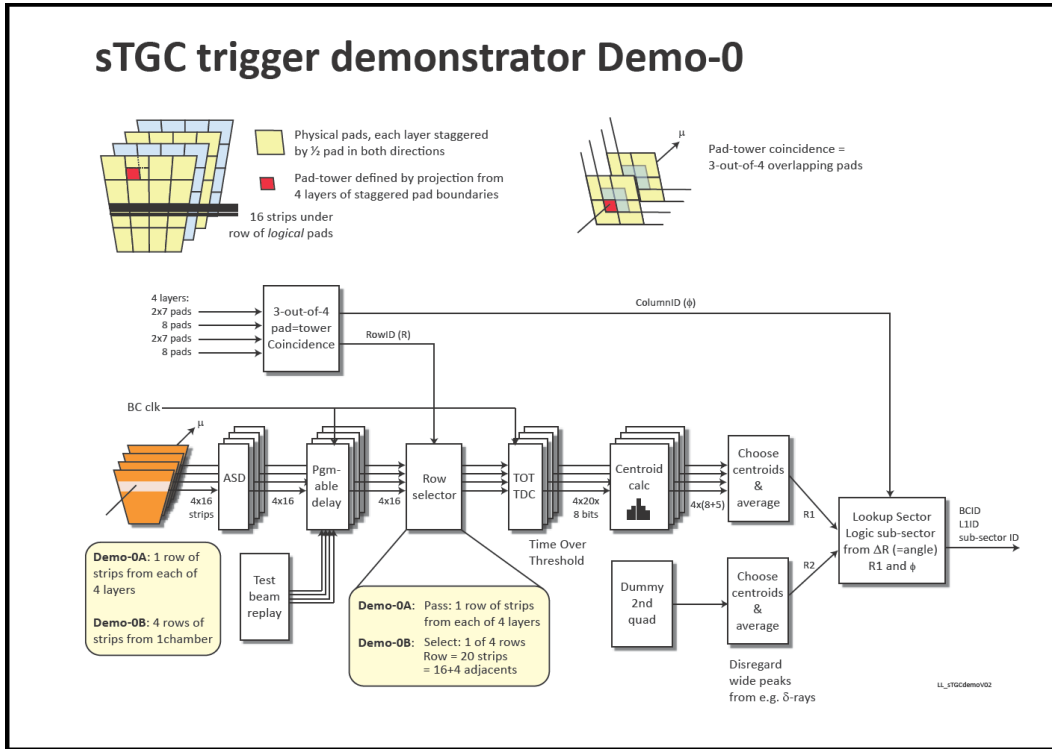

Figure 42: Block diagram of the sTGC trigger as presently implemented in an FPGA demonstrator.

C.2 Readout

The readout architecture will be the standard ATLAS readout with pipeline and derandomizer. The readout must support the requirements for commissioning, timing and problem diagnosis as well as the requirements for normal data taking. The current parameters and functionality of the GBT look appropriate.

- General Requirements:

    - Readout per pair of quadruplets, i.e. a tower
    - pipeline depth and rate for Phase II Level-1 trigger rate (500kHz) and latency.
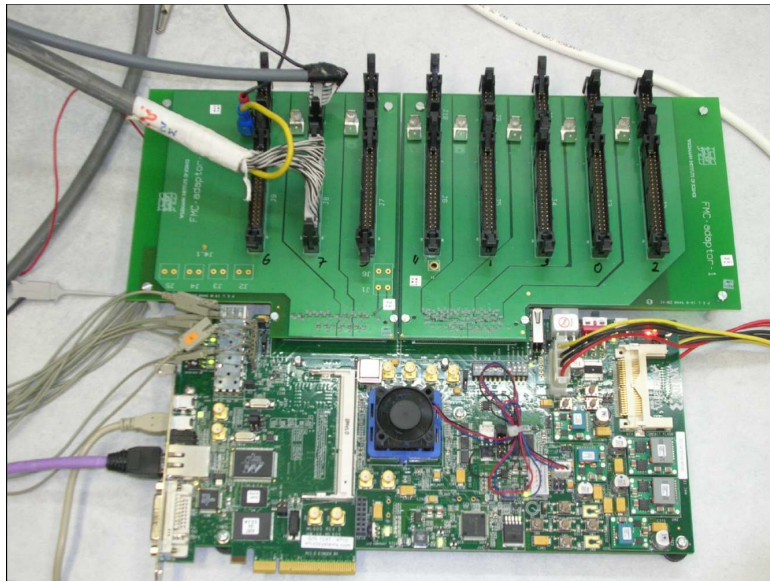
Figure 43: The trigger demonstrator board based on a commercial evaluation board (Xilynx ML605 with Virtex-6 FPGA). LVDS cables from eight TGC ASD modules are connected to the FPGA via custom mezzanine cards. These cards provide the required non-standard LVDS termination and merge power, threshold and test pulse lines from an external NIM module onto the cables to the ASDs. 64 strips and 44 pads are read out.
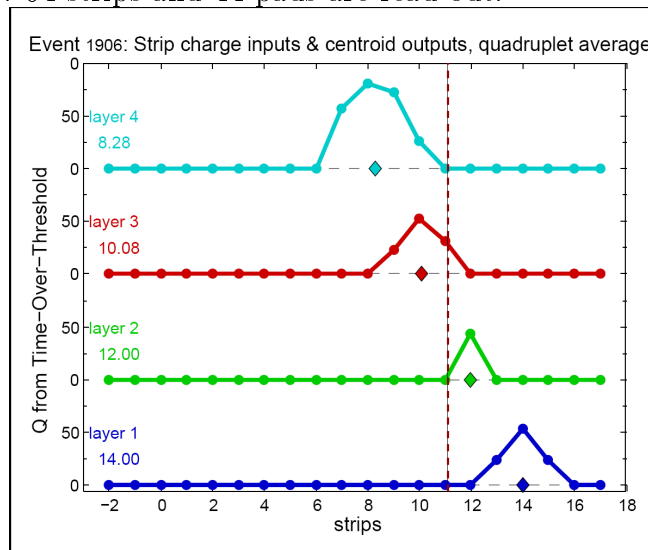

Figure 44: The four input strip profiles and the four calculated output centroids for a cosmic ray passing through a quadruplet. The centroid locations calculated by the demonstrator are on the left and are plotted as diamond symbols. The dashed line is the calculated average.

- Radiation tolerant

• Strip readout:

- converted Time-over-Thresholds of the selected strips in each layer (20*8*500kHz = 80Mb/s per layer) (Note that this means that channels not selected by the pad trigger will not be read out.)

- centroids per layer and the centroid averages (32-bits each)
- the extrapolated sub-sector on the Big Wheel (i.e. the input to the Sector Logic) (less than 16 bits)
- BCid (12-bits), L1Id (12-bits), source id (8-bits), etc.

- Pad readout:

  - pad hit pattern for each layer for the triggering BC, previous and next BCs. (about 80 pads per layer)

- Wire readout:

  - wire hit pattern for the selected wires in each layer, for the triggering BC, previous and next BCs. (about 70 wire-groups per layer)

The estimated data per trigger for a quadruplet is about 1600 bits. The GBT payload capacity of 3200 Mb/sec is easily sufficient for two quadruplets at a Level-1 trigger rate of 0.5 MHz.

C.3   Milestones for the sTGC electronics

The milestones for prototyping, development and production of the sTGC trigger electronics are given in Table 17.

Date	Milestone		
Aug. 2011	Demo-0	Goal	Demonstrate total latency, ASD to Sector Logic input, of pad local trigger, strip selection and sub-sector calculation from centroids in an FPGA.
		Includes	KEK TGC ASDs and Carioca ASDs, 4 layers of 16 strips, 4 layers of 8 or 14 pads, simple non-pipelined readout, based on commercial FPGA eval board
		Excludes	links and fibers, pipelined readout, rad tol technology
Jan. 2012	Demo-1	Goal	Add channels for full 8-layer logic, 64 strips per layer
		Includes	based on purpose built FPGA board
		Excludes	pipelined readout, rad tol technology
March 2012	Demo-1a	Goal	Run with BNL VMM Front End chip (ASD only)
Early 2012			Define on/off-chamber split and choose link hardware
			Design on-chamber boards
			produce rad tol ASICs for on-chamber part
			2nd spin of rad tol ASICs
			design off-chamber boards
			production of on- and off-chamber boards

Table 17: sTGC trigger development schedule

C.4 sTGC Construction and testing

The construction procedure of sTGCs follows very close the one used for the Big-Wheels TGC, where many new elements were introduced after completing the first 1,000 TGC chambers to increase the reliability of the detectors. This procedures include many QC steps, which correspond to 30% of the production steps. Furthermore, the Laboratory at the Weizmann Institute has been greatly improved by introducing a new resistive layer spraying Machine - see Fig. 45), as well as improvements in the wiring machine Fig. 46 (Right) and in the clean room (Fig. 46 (Left) to close the detectors.

Figure 45: New fully automatic graphite spraying machine recently installed at the Weizmann TGC facility, in a fully controlled Temperature and Humidity room.

Figure 46: Left: new clean room to close TGC detectors. Right: improved wiring machine at the Weizmann TGC facility.

These improvements were introduced for the production of spare detectors for the Japanese made TGCs that are presently being constructed, in collaboration with engineers from Shandong University (China), where 500 TGCs were made in the past, and were there is a strong interest to continue the previous collaboration. Similarly, groups from Argentina and Chile

would be interested in a possible collaboration, if the project is approved, which would allow to start a real hardware activity in these countries. The final quality control procedure will be performed at the renewed Cosmic-Ray facilities at the Technion and Tel-Aviv University (see Fig. 47), where every detector is scanned with cosmic rays. The final test, which has proven extremely effective in the detectors that were so tested, will be to irradiate them for half an hour in a new CO(60) irradiation facility that has been constructed at the SOREQ nuclear Center. This test is crucial to find any possible defects in a given detector.

Figure 47: Renewed TGC Test-bench facility at Tel Aviv University.

C.5 sTGC cost estimate

The present cost estimates for the mechanical parts are based on the production of spare detectors, and although the quantities are smaller, and therefore the basic costs could go down, the sTGCs will require additional work, due to the larger number of channels, therefore these values could be taken as a reasonable estimate. The break-down of the total number of detectors and their dimensions are given in Table 18, while in Table 19, the expected costs for the Mechanics, Transport and testing are given. These costs include also local taxes and manpower, which are not part of the CORE estimates. Possible overheads by the institutions are not included. The expected cost of the electronics (including trigger) are given in a separate table

Chamber type	Appr. Dimensions	# Modules-side	Gas-gaps-size
EIL0	1007x1094 (sub 2 W)	16	2x64 ganged
EIL1	1679x1275	16	64
EIL2	2050x1275	16	64
EIS0	715x1275 (sub 2W)	16	2x64 ganged
EIS1	1080x1275	16	64
EIS2	1524x1094	16	64
Total		96	384
Total 2 sides		192	768

Table 18: break-down of the number of mechanical units and their respective number of gas-gaps.

Item	CORE cost	TAX& Overheads	Total
Raw material	580	97	677
Machining of part	518	85	603
Wire	330	54	384
Transport	60	10	70
Cosmic test	180		180
Radiation test	70		70
Tools	80	13	93
Manpower		1500	1500
Equipment	41	7	48
Total	1859	1766	3625

Table 19: Mechanical and testing costs (in kCHF) of the production of 768 sTGCs gas-gaps.

References

[1] G. Aad et al. Expected Performance of the ATLAS Experiment - Detector, Trigger and Physics. 2009.

[2] G. Aad et al. The ATLAS Experiment at the CERN Large Hadron Collider. *JINST*, **3** S08003 (2008)

[3] M. Bosman et al. Estimation of Radiation Background, Impact on Detectors, Activation and Shielding Optimization in ATLAS, ATLAS Note *ATL-GEN-2005-001* (2005)

[4] P. Barrow, G. Conti, M. Franklin and L. Jeanty, Cavern Background, Muon Upgrade meeting, july, 29th, 2011 *https://indico.cern.ch/congerenceDisplay.py?confId=148910*

[5] Y. Arai et al., ATLAS Muon Drift Tube Electronics, *JINST* **3** P09001 (2008)

[6] J. Christiansen et al., Manual and User Application Notes for the HPTDC, (2004), *http://tdc.web.cern.ch/tdc/hptdc/docs/hptdc_manual_vs2.2.pdf* and *http:/tdc.web.cern.ch/ tdc/hptdc/hptdc.htm*

[7] Posch C., Hazen E., Oliver J., MDT-ASD User's Manual, (2007), ATL-MUON-2002-003; *https://edms.cern.ch/document/899037/2/ASD_Manual_vs_2007.pdf*

[8] Y. Arai, *AMT-3 User Manual*, *https://edms.cern.ch/file/897562/1/AMT3manual_033.pdf*, *http://atlas.kek.jp/tdc/amt3/AMT3manual_033.pdf*

[9] P. Moreira, find some reference to the GBT!!

[10] M. Deile et al., *Performance of the ATLAS Precision Muon Chambers under LHC Operating Conditions*, Proceedings of the 9th Pisa Meeting on Advanced Detectors, Isola d'Elba, Italy, 25–31 May 2003, Nucl. Instr. and Methods **A518** (2004) 65;
M. Deile et al., *Resolution and Efficiency of the ATLAS Muon Drift-Tube Chambers at High Background Rates*, Proceedings of the 10th Vienna Conference on Instrumentation, Vienna, Austria, 16–21 February 2004, Nucl. Instr. and Methods **A535** (2004) 212;
S. Horvat et al., *Operation of the ATLAS Muon Drift-Tube Chambers at High Background Rates and in Magnetic Fields*, IEEE Transactions on Nuclear Science, Vol. 53, No. 2 (2006) 562.

[11] J. Dubbert et al., *Development of Precision Drift Tube Detectors for the Very High Background Rates at the Super-LHC*, Proceedings of the 2007 IEEE Nuclear Science Symposium, Honolulu, Hawaii, USA, 28 October–2 November 2007; MPI report, MPP-2007-172, November 2007.

[12] M. Deile *et al.*, *Performance of the ATLAS Precision Muon Chambers under LHC Operating Conditions*, Nucl. Instr. and Meth. **A 518** (2004) 65; M. Deile *et al.*, *Resolution and Efficiency of the ATLAS Muon Drift-Tube Chambers at High Background Rates*, Nucl. Instr. and Meth. **A535** (2004) 212.

[13] S. Horvat *et al.*, *Operation of the ATLAS Precision Muon Drift-Tube Chambers at High Background Rates and in Magnetic Fields*, IEEE trans. on Nucl. Science Instr. Vol. 53, 2 (2006) 562.

[14] B. Bittner *et al.*, *Development of Precision Muon Drift Tube Detectors for the High-Luminosity Upgrade of the LHC*, Nucl. Phys. B (Proc. Suppl.) **215** (2011) 143.

[15] B. Bittner *et al.*, *Development of Muon Drift-Tube Detectors for High-Luminosity Upgrades of the Large Hadron Collider*, Nucl. Instr. and Meth. **A617** (2010) 169.

[16] R. Veenhof, *GARFIELD: Simulation of Gaseous Detectors, Version 8.01, CERN*, write-up: http://wwwinfo.cern.ch/writeup/garfield.

[17] W. Riegler, *High Accuracy Wire Chambers*, Nucl. Instr. and Meth. **A 494** (2002) 173.

[18] B. Bittner *et al.*, *Development of Fast High-Resolution Muon Drift-Tube Detectors for High Counting Rates*,
Nucl. Instr. and Meth. **A 628** (2011) 154.

[19] M. Aleksa *et al.*, *Rate Effects in High-Resolution Drift Chambers*, Nucl. Instr. and Meth. **A 446** (2000) 435.

[20] O. Kortner *at al.*, *Alignment of the ATLAS Muon Spectrometer with Tracks and Muon Identification at High Background Rates*, Nucl. Instr. and Meth. **A581** (2007) 545-548.

[21] H. Kroha, *Quality Assurance and Quality Control Reference Document for ATLAS MDT Chamber Construction*, ATLAS Note, ATL-MUON-2000-008, May 1999.

[22] S. Horvat, O. Kortner, H. Kroha, *Determination of the Spatial Drift-Tube Resolution Using Muon Tracks*, ATLAS Note, ATL-MUON-PUB-2006-008, July 2006.

[23] G. Conti, P. Barrow, M. Franklin and L. Jeanty, *Cavern Background Studies from MDT*, https://indico.cern.ch/getFile.py/access?contribId=2&resId=0&materialId=slides&confId=151320

[24] J. Dubbert, S. Horvat, O. Kortner, H. Kroha, R. Richter, *Upgrade of the ATLAS Muon Trigger for the SLHC*, *JINST* **5** C12016 (2010)